

Measurement of  $B \rightarrow J/\psi\eta K$  decay branching fraction  
and search for narrow resonances in  $J/\psi\eta$  final state

2013

School of Interdisciplinary Research of Scientific Phenomena  
and Information  
Nara Women's University

Tomoko Iwashita  
Doctorial thesis

### Abstract

We measured branching fractions of  $B \rightarrow J/\psi\eta K$  decay. These results are obtained from a data sample that contains  $772 \times 10^6$   $B\bar{B}$  pairs collected near the  $\Upsilon(4S)$  resonance with the Belle detector at the KEKB asymmetric  $e^+e^-$  collider. We get the branching fractions  $\mathcal{B}(B^\pm \rightarrow J/\psi\eta K^\pm) = (1.3 \pm 0.1(\text{stat.}) \pm 0.1(\text{syst.})) \times 10^{-4}$ ,  $\mathcal{B}(B^0 \rightarrow J/\psi\eta K_S^0) = (4.3 \pm 0.7(\text{stat.}) \pm 0.4(\text{syst.})) \times 10^{-5}$ . And we observed upper limit of  $\mathcal{B}(B^\pm \rightarrow X(3872)(\rightarrow J/\psi\eta)K^\pm) < 3.8 \times 10^{-6}$ .  $X(3872)$  state is discovered by Belle in 2003 and candidate of exotic state. We search  $X(3872)$ 's  $C$ -odd partner in a tetra-quark model using  $B \rightarrow J/\psi\eta K$  decay system.

## Acknowledgements

In order to make this thesis, I would like to thank all the people who were involved.

First and foremost, I wish to express my gratitude to my supervisor, Prof. K. Miyabayashi and Dr. V. Bhardwaj.

And thank you for your help, Prof. H. Hayashii and Prof. S. Noguchi.

Moving on to KEK, I'd like to thank Prof. Y. Sakai, Prof. Y. Ushiroda, Prof. T. Karim, Prof. S. Nishida, Prof. M. Nakao.

I'd like to thank Dr. J. Brodzicka, Dr. A. Zupank, and my Belle Note's referees Prof. A. Bondar, Prof. M. C. CHANG, Prof. I. Adach and other charm group members.

At last, I want to thank my family and friends who have supported me.



# Contents

<b>1</b>	<b>Introduction</b>	<b>1</b>
1.1	Electroweak interactions and $B$ meson decays	3
1.2	Quark model and formation of hadrons	4
1.3	Charmonium	6
1.3.1	Multiquarks	7
1.3.2	Hybrids	8
1.3.3	Threshold effects	9
1.4	$X(3872)$ state	9
<b>2</b>	<b>The Belle experiment</b>	<b>13</b>
2.1	The KEKB accelerator	13
2.2	The Belle detector	14
2.2.1	Beampipe	15
2.2.2	Silicon Vertex Detector (SVD)	17
2.2.3	Central Drift Chamber (CDC)	18
2.2.4	Aerogel Cerenkov Counter (ACC)	20
2.2.5	Time of Flight Counter (TOF)	22
2.2.6	Electromagnetic Calorimeter (ECL)	23
2.2.7	Solenoid Magnet	24
2.2.8	$K_L^0$ and Muon Detector (KLM)	25
2.2.9	Trigger and Data Acquisition	28
<b>3</b>	<b>Event selection for <math>B \rightarrow J/\psi\eta K</math> decays</b>	<b>33</b>
3.1	Data sample	33
3.2	Reconstruction and identification of particles	34
3.2.1	Charged particle detection	35
3.2.2	Shower reconstruction and photon selection	35
3.2.3	$B\bar{B}$ event selection	35

3.2.4	$\mu, e$ identification . . . . .	36
3.2.5	Kinematic fit . . . . .	36
3.2.6	$J/\psi$ reconstruction . . . . .	37
3.2.7	$\eta$ reconstruction . . . . .	37
3.2.8	$K/\pi$ identification . . . . .	39
3.2.9	$K_S^0$ reconstruction . . . . .	40
3.3	Reconstruction of $B \rightarrow J/\psi\eta K$ . . . . .	40
3.4	Detection efficiency of $B \rightarrow J/\psi\eta K$ decays . . . . .	42
3.4.1	$B^\pm \rightarrow J/\psi\eta K^\pm$ mode . . . . .	42
3.4.2	$B^0 \rightarrow J/\psi\eta K_S^0$ mode . . . . .	43
<b>4</b>	<b>Background study</b> . . . . .	<b>45</b>
4.1	Continuum background reduction . . . . .	45
4.2	Main backgrounds . . . . .	45
4.2.1	$\psi' \rightarrow J/\psi\pi^+\pi^-$ and $\chi_{c1}(\chi_{c2}) \rightarrow \gamma J/\psi$ veto . . . . .	46
4.2.2	Non $J/\psi$ background . . . . .	48
4.3	Optimization of $\Delta E$ window . . . . .	49
4.4	Background probability density functions . . . . .	50
<b>5</b>	<b>Results and discussions</b> . . . . .	<b>53</b>
5.1	$B$ decay signal extraction . . . . .	53
5.2	Resolving intermediate states by $M_{J/\psi\eta}$ distribution . . . . .	53
5.3	Correction and systematic uncertainties . . . . .	55
5.3.1	Tracking efficiency systematic . . . . .	55
5.3.2	Correction and systematic uncertainty of $K$ ID . . . . .	56
5.3.3	Correction and systematic uncertainty of $\mu$ ID . . . . .	56
5.3.4	Electron ID correction and systematic uncertainty . . . . .	56
5.3.5	$\eta$ detection systematic uncertainty . . . . .	57
5.3.6	Correction and systematic uncertainty of $K_S^0\pi^+\pi^-$ de- tection . . . . .	57
5.3.7	Signal MC statistics . . . . .	57
5.3.8	Number of $B$ meson pairs . . . . .	58
5.3.9	Branching fraction uncertainties . . . . .	58
5.3.10	PDF systematic uncertainties . . . . .	58
5.3.11	Summary of systematic uncertainties . . . . .	58
5.4	Upper limit for resonance in $J/\psi\eta$ final state . . . . .	59
5.4.1	$X(3872)$ . . . . .	59
5.4.2	Narrow resonances at other mass points . . . . .	59

*CONTENTS*

7

**6 Summary**

**63**



# Chapter 1

## Introduction

The development of particle physics over the past century has led to what is called the Standard Model (SM) of particle physics. This framework is based on the renormalizable quantum field theory and gives descriptions for the fundamental particles of matter, leptons (electrons, muons, taus, and their associated neutrinos) and quarks (with "flavors" up, down, charm, strange, top, and bottom), as well as their interactions via the electromagnetic, strong, and weak forces mediated by photons, gluons, and the  $W$  and  $Z$  bosons, respectively. Weak interactions are capable of changing quark flavor in the charged current cases and the couplings between quark flavors are described by the Cabibbo-Kobayashi-Maskawa (CKM) matrix [1]. The SM also predicts the existence of the Higgs boson that is responsible for the masses of the other particles in the SM, thought to be the consequence of the symmetry breaking of the electromagnetic and weak forces. In the SM, quarks are massive point-like particles that interact with one another predominantly via the strong force. The strong force is mediated by gluons and acts between quarks that have colour, the strong force analogue of electromagnetic charge. The theory describing these processes is called quantum chromodynamics (QCD). The QCD predicts the phenomena called "asymptotic freedom" that means the coupling gets smaller in higher energy scale, i.e. in shorter distance [2]. It is confirmed by experiments and is recognized as one of the remarkable successes of the SM. It also essentially explains how quarks bind together to form matter as hadrons. One unsolved question is why hadrons are predominantly formed to be baryons or mesons which contain three constituent quarks or constituent quark-antiquark, respectively. In spite of the fact there is no explicit suppression rule to form other constituent quark configurations

in QCD, the number of candidate states for unusual structure hadrons is still limited.

From 1999, LEPS experiment at SPring-8 and Belle experiment at KEK B-factory started physics runs and in 2003 those experiments reported the pentaquark candidate  $\Theta(1540)^+$  in  $K^+n$  [5] and the extraordinary narrow charmonium-like resonance  $X(3872)$  in  $J/\psi\pi^+\pi^-$  [4], respectively.  $X(3872)$  is an exotic hadron candidate, thought to be a tetra-quark or a meson-meson molecule state as discussed in more detail later. Since  $X(3872)$  was explored in  $B^\pm \rightarrow J/\psi\pi^+\pi^-K^\pm$  decay, other multi-body  $B$  meson decays are also thought to be the place to visit. This work focuses on three-body  $B$  meson decays,  $B^\pm \rightarrow J/\psi\eta K^\pm$  and  $B^0 \rightarrow J/\psi\eta K_S^0$  modes. Measurements of branching fraction for these decay modes essentially provide new knowledge about  $B$  meson property. In addition, the  $J/\psi\eta$  system in these decays provide a chance to search for a charmonium or a charmonium-like exotic hadron. The charmonium-like exotic hadrons are identified by comparing their characteristics with the ordinary charmonium. The experimental data taken at a  $B$ -factory have rich statistics of the hadrons containing heavy flavored quarks,  $b$  or  $c$ . Contrary to the case of hadrons comprised by light quarks ( $u$ ,  $d$  and  $s$ ) where mixing of neutral mesons plays an important role because of  $SU(3)$  flavor symmetry,  $c$  and  $b$  quarks are well separated from other quark flavor due to their large masses of approximately  $1.5 \text{ GeV}/c^2$  and  $5 \text{ GeV}/c^2$ , respectively. Therefore the relation between the observed state and its constituent quarks wave function is pretty straight-forward. Especially, charmonium ( $c\bar{c}$ ) and bottomonium ( $b\bar{b}$ ) cases, a QCD potential model works well to predict their masses including excited states because their large quark masses are functioning as a kind of good cut off.

The charmonia which are lower than the open charm ( $D\bar{D}$ ) threshold can decay only weak, electromagnetic and strong but OZI-suppressed processes, thus they have narrow decay width. On the other hand, above  $D\bar{D}$  threshold,  $3740 \text{ MeV}/c^2$ , strong decay to the  $D$  meson pair predominantly takes place and it results in wide decay width. Therefore, when a charmonium-like hadron has larger mass than the open charm threshold and having one of the following characteristics, it is to be recognized as an exotic hadron candidate; (1) decay branching fraction other than  $D\bar{D}$  is large, (2) unusual narrow decay width, (3) the special decay mode which can not be explained as  $c\bar{c}$  and (4) mass does not match any predicted states.

In  $X(3872)$  case, in spite of the fact that it has larger mass than  $D\bar{D}$  threshold, it decays to  $J/\psi\pi^+\pi^-$ , decay width is very narrow and its mass does not

match with any predicted masses of still unconfirmed charmonium states. After its discovery, search for the decay into  $J/\psi\eta$  was attempted in relatively early stage. BaBar collaboration reported an upper limit on the product of branching fractions,  $\mathcal{B}(B \rightarrow X(3872)K)\mathcal{B}(X(3872) \rightarrow J/\psi\eta) < 7.7 \times 10^{-6}$  with the data sample corresponding to integrated luminosity of  $82 \text{ fb}^{-1}$  [7]. This result is based on limited data statistics and so far no one has revisited this final state.

In recent a few years, since the radiative decay  $X(3872) \rightarrow J/\psi\gamma$  has been established [8, 9], the  $X(3872)$ 's charge conjugation parity,  $C$ , is confirmed to be even ( $C = +1$ ). The  $J/\psi\eta$  final state has  $C$ -odd ( $C = -1$ ), thus search for narrow resonance in this final state does not mean an attempt to look for new  $X(3872)$  decay mode but seeking an its  $C$ -odd partner state, which is predicted generally in either tetra-quark or meson-meson molecule hypothesis. This work is based on a data sample containing  $772 \times 10^6$   $B\bar{B}$  pairs collected by the Belle detector at the KEKB energy-asymmetric  $e^+e^-$  collider by the completion of their operation at 2010 June 30th. It corresponds to nine times larger statistics than that for the BaBar published analysis, therefore we may reveal a signature of  $X(3872)$ 's  $C$ -odd partner, or put more stringent constraint for that state.

In this chapter, physics about quarks and hadrons are reviewed in more detail, including exotic hadrons. After that, experimental apparatus is explained and finally the analysis to get branching fractions for three-body  $B$  decays into  $J/\psi\eta K$  as well as to search for narrow resonances in the  $J/\psi\eta$  final state are presented.

## 1.1 Electroweak interactions and $B$ meson decays

In the SM, the electromagnetic and the weak interactions are unified as the field theory based on  $SU(2) \times U(1)$  gauge symmetry. Between electrically charged particles, photons ( $\gamma$ ) are exchanged to cause electromagnetic interaction phenomena. Among three weak bosons, the  $Z^0$  is responsible for the neutral current interaction and its mass is  $91.19 \text{ GeV}/c^2$ . Because of the electroweak mixing that is denoted as  $\sin\theta_W$ , the interference between  $\gamma$  and  $Z^0$  exchange diagrams takes place and the resultant forward-backward

asymmetries in charged fermion pair production are well confirmed by the high energy  $e^+e^-$  collision experiments at the center mass energy around 100 GeV. The remained two weak bosons,  $W^+$  and  $W^-$  are taking part in the charged current interaction and thus it changes the flavor of quarks and leptons. Since  $B$  meson is the ground state  $b$  hadron, all its experimentally confirmed decay modes are only caused by the charged current interaction. The charged current weak interaction in quark sector is described by the Kobayashi-Maskawa theory [1]. The couplings between different quark flavors are described as a quark-mixing matrix. The quark-mixing matrix is written as [3];

$$\begin{pmatrix} V_{ud} & V_{us} & V_{ub} \\ V_{cd} & V_{cs} & V_{cb} \\ V_{td} & V_{ts} & V_{tb} \end{pmatrix} = \begin{pmatrix} 1 - \lambda^2/2 & \lambda & A\lambda^3(\rho - i\eta) \\ -\lambda & 1 - \lambda^2/2 & A\lambda^2 \\ A\lambda^3(1 - \rho - i\eta) & -A\lambda^2 & 1 \end{pmatrix}. \quad (1.1)$$

The  $B$  meson decays into the final state with a charmonium is dominantly caused by  $b \rightarrow c\bar{c}s$  transition in the quark level. Here, since both relevant couplings  $V_{cb}$  and  $V_{cs}$  are the favored ones, large amount of  $B$  meson decay data contain high statistics charmonium sample in the final states. This holds not only for two-body  $B$  decay modes such as  $J/\psi K^{(*)}$ ,  $\psi(2S)K^{(*)}$  and so on, but also three-body modes including the  $J/\psi\eta K$  which is the target of this work. Because of relatively heavy  $B$  meson mass, the decay daughters get quickly apart in the two-body decays thus there is very small final state interactions. This picture is called "factorization". On the other hand there can be several intermediate states in the three(or more)-body decays and this fact provides us a possibility to hunt a charmonium-like exotic hadrons in many-body  $B$  decay processes as one of the intermediate states. In the following subsections, the quark model, hadron formation and several exotic hadron models are discussed.

## 1.2 Quark model and formation of hadrons

Quarks are acting as building blocks to form composite particles called hadrons. Because of the strong interaction field, quarks are confined in hadrons and can not go alone through vacuum. Quarks and gluons have an additional quantum number called colour charge, which characterizes three states, "red", "green" and "blue". A quark can take one of the three colours, while an antiquark takes an anticolour. Gluons carry both a colour and an anticolour.

The colour confinement principle requires hadrons to be colourless. As a consequence, there are two common types of hadrons, baryons and mesons. Baryons are hadrons with half-integer spin and contain three constituent quarks. Nucleons, proton and neutron are the ground state baryons comprised by  $u$  or  $d$  quarks only. Note that the bare masses of  $u$  and  $d$  quarks are not one third of the nucleon mass. Inside hadron, there is a large effect from the many virtual quark-antiquark pairs and gluons that do not give any net quantum numbers but make hadron more massive than the sum of the masses of the valence quarks which carry the net quantum numbers. Mesons are hadrons having integer spin and composed of a quark-antiquark pair and thus have zero baryon number. Each meson has a corresponding antimeson, where quarks are replaced by their corresponding antiquarks and. For example, the  $B^0$  particle is a bottom meson, composed of a down quark and a bottom antiquark. Similarly, the  $B^\pm$  meson is composed of an up quark and a bottom antiquark. Since mesons have integer spin, some light mesons can act as the bosons which mediate strong force in relatively long distance,  $\sim 10^{-14}$ m. As well known,  $\pi$  exchange between nucleons can be a good picture to describe nuclear forces to form a nuclei. This is because the pion is a Nambu-Goldstone boson coming from  $SU(3)$  symmetry breaking of strong interaction at low energy. Another example would be the "Vector Meson Dominance" that means neutral light vector mesons such as  $\rho^0$ ,  $\omega$  and  $\phi$  can strongly couple with photons. The vector meson dominance is known to largely contribute to the hadron production in photon-photon collisions especially at relatively low transverse momentum region. These characteristics for the light mesons are due to the flavor mixing among  $u$ ,  $d$  and  $s$  by  $SU(3)$  flavor symmetry. For example, in the case of  $\eta$  and  $\eta'$ , using one of the flavor octet  $\psi_8 = (u\bar{u} + d\bar{d} - 2s\bar{s})\sqrt{6}$  and the flavor singlet  $\psi_1 = (u\bar{u} + d\bar{d} + s\bar{s})\sqrt{3}$  as well as the mixing angle  $\theta$ ,  $\eta = \psi_8 \cos\theta - \psi_1 \sin\theta$  and  $\eta' = \psi_8 \sin\theta + \psi_1 \cos\theta$ . Therefore we have to solve these relations to understand constituent quarks wave function in the observed meson states.

As briefly mentioned before, heavy flavored hadrons are well separated from light quark sectors because of the much larger masses. Therefore the relation between the observed states and its corresponding wavefunction is much more straight-forward. This really holds well in the case of the quarkonium which is composed of a heavy quark and its antiquark. It is called a bottomium if it is a  $b\bar{b}$  meson, such as the  $\Upsilon(4S)$  produced at Belle; or a charmonium when it is a  $c\bar{c}$  meson like the  $J/\psi$ . Charmonium states have masses around  $3 \text{ GeV}/c^2$ , and bottomium states around  $10 \text{ GeV}/c^2$ . The toponium doesn't

exist, because the top quark is so heavy that it decays before a bound state can form.

### 1.3 Charmonium

As already explained, a charmonium is a  $c\bar{c}$  meson and the diagram of the known charmonium and apparently charmonium-related states are shown in Fig 1.1. The quantum numbers and basic properties of most of the states in the charmonium family can be described within a simple picture of a nonrelativistic quark-antiquark pair  $c\bar{c}$ . In this picture the states are characterized by the orbital angular momentum  $L$ , the total spin  $S$  of the quark pair, and the total angular momentum  $J$ , which defines the spin of the state viewed as a particle. As usual, the total angular momentum is given by the vector sum of the orbital and the spin momenta;  $\vec{J} = \vec{L} + \vec{S}$ . Likewise, the total spin  $S$  is determined by the vector sum of the quark and antiquark spins;  $\vec{S} = \vec{s}_c + \vec{s}_{\bar{c}}$ . Clearly,  $S$  takes the values 0 and 1, thus splitting the four possible spin states of the pair into a singlet and a triplet. Furthermore, the excitation of the radial motion of the  $c\bar{c}$  pair results in a spectrum of levels with the same  $L$ ,  $S$  and  $J$ , and differing by the radial quantum excitation number  $n_r$ . With  $n_r = 0$  corresponding to the lowest state. It is therefore customary to encode the values of these quantum numbers for each state of charmonium in the form of the symbol  $(n_r + 1)^{(2S+1)}L_J$ .

The combination  $2S + 1$  conveniently indicates the spin multiplicity, while following the tradition from atomic physics the values of  $L = 0, 1, 2, 3$  are written as  $S, P, D, F$ . In this notation the lowest state with  $L = 0$ ,  $S = 0$  and (necessarily)  $J = 0$  is represented as  $1^1S_0$  ( $\eta_c$  resonance) while the first excited state with the same quantum numbers is  $2^1S_0$  ( $\eta'_c$ ). The value of  $L$  determines the parity ( $P$ ) for each of the states;  $P = (-1)^{L+1}$ , while  $L$  and  $S$  combined also determine the charge conjugation parity;  $C = (-1)^{L+S}$ . Therefore the previously mentioned  $1^1S_0$  states have quantum numbers  $J^{PC} = 0^{-+}$ , while e.g.  $3^1S_1$  states have the same quantum numbers  $J^{PC} = 1^{--}$  as the electromagnetic current, so that these states for example  $J/\psi$ ,  $\psi'$ ,  $\psi(3770)$  and so on, can be produced as resonances in  $e^+e^-$  annihilation. The states having other quantum numbers than  $J^{PC} = 1^{--}$  have been mostly confirmed by the decay from the higher vector states. For example,  $S = 1$ ,  $L = 1$  and  $n_r = 0$  result in three states called  $\chi_{c0}$ ,  $\chi_{c1}$  and  $\chi_{c2}$  according to each own  $J$  and all of them can be found in  $\psi$ 's radiative decays. So far, all the states be-

low  $D\bar{D}$  threshold ( $3740 \text{ MeV}/c^2$ ) are identified. On the other hand, there are still unconfirmed states above this threshold and several charmonium-like states having unusual characteristics have been reported. Here, some typical ordinary charmonia heavier than  $D\bar{D}$  threshold would be reviewed. As already mentioned, usually strong decays to open charm mesons become dominant thus decay widths are wide. Actually  $\psi(3770)$  dominantly decays into  $D\bar{D}$  and its decay width is  $27 \text{ MeV}$  while  $J/\psi$  and  $\psi'$  have widths of  $93 \text{ keV}$  and  $300 \text{ keV}$ , respectively. For a charmonium-like hadron, difference from the typical properties implies a possibility of exotic hadron. For plausible pictures of charmonium-like exotic hadrons are described in the following subsections.

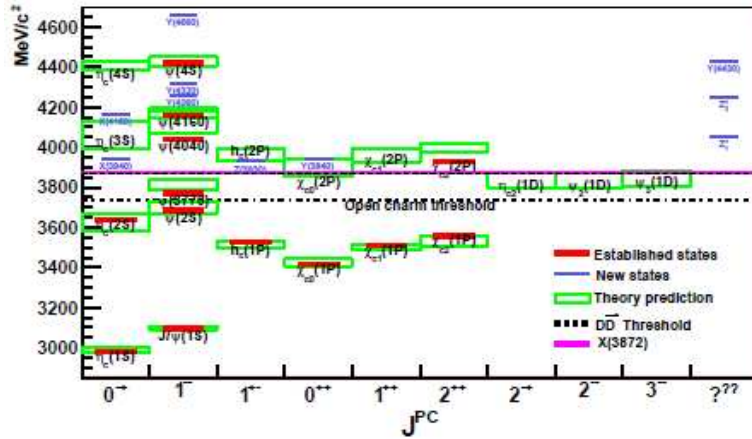


Figure 1.1: Charmonium spectrum. The masses are shown as a function of the quantum number,  $J^{PC}$ .

### 1.3.1 Multiquarks

People can say why we have only two quarks (one quark and another anti-quark) or three quarks (different colors) to make up the matter. There are more combinations possible. Multiquark model supports such hypothesis. Originally, in 1970s, the idea of such a particle known as tetra-quark was considered to explain the properties of light scalar mesons  $f_0(600)$ ,  $f_0(980)$ , and  $a_0(980)$  as their properties were not well explained by the existing quark model) [10]. Two types of multiquark states have been considered. The

first is a molecular state (also known as deuson) which comprises of two charmed mesons bound together to form a molecule. Molecular states are loosely bound and are expected to bind through two mechanism; quark/color exchange interactions at short distance and pion exchange at large distance (expected to dominate). Mesons inside the molecule are weakly bound, so they decay as if they are free. Also, molecular states are not isospin eigenstates which result in distinctive decay patterns. The idea of molecular states was initially used to explain an excessively large  $D^*\bar{D}^*$  production cross section compared with the  $D\bar{D}$  and  $D^*\bar{D}^*$  production cross sections at the peak of  $\psi(4040)$  in  $e^-e^+$  annihilation. It was supposed that  $\psi(4040)$  can be a  $P$ -wave molecular resonance in the  $D^*\bar{D}^*$  system and was forgotten but was revived in 2003 after the discovery of the  $X(3872)$  particle [4].

Multiquark state can also exist in the form of a tightly bound four-quark state (known as tetra-quark) and they are expected to have properties different from those of a molecular state because size and proper degree of freedom for the description are different. Maiani et al. [11] suggested that the tetra-quark can be described as a diquark-diantiquark structures in which the quarks group into color-triplet scalar and vector clusters and the interactions are dominated by a simple spin-spin interaction. The strong decays are expected to proceed via rearrangement processes, followed by disassociation, that give rise to the decays such as  $X(3872) \rightarrow \rho J/\psi \rightarrow \pi\pi J/\psi$  or  $X(3872) \rightarrow D\bar{D}^* \rightarrow D\bar{D}\gamma$  for example. A prediction that distinguishes multiquark states containing a  $c\bar{c}$  pair from conventional charmonia is the possible existence if multiplets that include members with nonzero charge (e.g.  $[cu\bar{c}\bar{d}]$ ), strangeness (e.g.  $[cd\bar{c}\bar{s}]$ ), or both (e.g.  $[cu\bar{c}\bar{s}]$ ). In tetraquark picture, Terasaki [12] suggested a  $C$ -odd state can decay to  $J/\psi\eta$ . It is important to revisit this final state with high statistics data.

### 1.3.2 Hybrids

Hybrid mesons are states which has an excited gluon degree of freedom. Such states are discussed in many different models and calculation schemes. In lattice QCD, the quarks are viewed as moving in adiabatic potentials produced by gluons in analogy to the atomic nuclei in molecules moving in the adiabatic potentials caused by electrons. Conventional charmonium spectrum is produced by lowest adiabatic surfaces while excited adiabatic surfaces lead to an octet of the lightest hybrids. These excitations introduces an additional degree of freedom related to gluons and add the spin and the angular

momentum [13, 14]. In the flux-tube model[15], the lowest excited adiabatic surfaces corresponds to transverse excitations of the flux tube and leads to a doubly degenerate octet of the lowest mass hybrids with quantum numbers  $J^{PC} = 0^{+-}, 0^{-+}, 1^{+-}, 1^{-+}, 2^{+-}, 2^{-+}, 1^{++},$  and  $1^{--}$ . Some of the octet component having quantum numbers  $0^{+-}, 1^{-+},$  and  $2^{+-}$  are not possible for  $c\bar{c}$  bound states in the usual quark model. If these states are observed, they will confirm the existence of an unconventional states. Lattice QCD predicts the lowest charmonium hybrid state to be roughly  $4200 \text{ MeV}/c^2$  in mass [16].

### 1.3.3 Threshold effects

In addition to these states, threshold can also give rise to the structures in cross sections and kinematics distributions. The possible thresholds include the  $DD^*, D^*D^*, DD_1$  and  $D^*D_1$  at  $E_{cm} \sim 3872, 4020, 4287$  and  $4430 \text{ MeV}$ , respectively.  $S$ -wave ( $L = 0$ ) scattering dominates the cross section at the threshold, however in few cases higher waves also become important. States in a relative  $S$ -wave with little relative momentum can live long on the timescale of strong interactions, then have enough time to exchange pions to interact each other [17]. Here, molecular state is possible to be produced due to the possible binding via an attractive  $\pi$  exchange which could occurs through couplings such as  $D\pi^0 \leftrightarrow D^*$ . It should be noted that there could also be a repulsive interaction which arises due to some strong interaction effects and it can result in a virtual state above threshold. Thus, near the kinematical threshold there can be a structure in the cross section which may or may not be a simple real resonance. In addition, if there are  $c\bar{c}$  states which are near a threshold, they can interact with the threshold and will result in a mass shifts of both the  $c\bar{c}$  resonance and the threshold-related enhancement. This effects could be quite significant in the observed cross section, particularly for the  $c\bar{c}$  states close to the thresholds [17, 18].

## 1.4 $X(3872)$ state

In 2003, the Belle Collaboration discovered a narrow charmonium-like state  $X(3872) \rightarrow J/\psi\pi^+\pi^-$  having width less than  $2.3 \text{ MeV}/c^2$  (90% C.L.) and a mass of  $3872.0 \pm 0.6 \pm 0.5 \text{ MeV}/c^2$  in the charged  $B$  decay to  $X(3872)$  and  $K$  [6]. Later on it was confirmed by CDF [19], D0 [20], LHCb [21] and BaBar [22] Collaborations. Figure 1.2 shows observation of  $X(3872)$  at Belle. At present

the world average width and mass are  $\Gamma < 1.2 \text{ MeV}/c^2$  and  $3871.7 \pm 0.2 \text{ MeV}/c^2$  in which Belle experiment is dominating [26]. Since  $X(3872) \rightarrow J/\psi\pi^+\pi^-$ , it is quite obvious to identify  $X(3872)$  as the new charmonium state. The  $X(3872)$  displays some characteristics of a charmonium-like state, but its narrow width above the  $D\bar{D}$  threshold and quantum numbers limit its possible assignment within the charmonium model. Its mass near  $m_{D^0} + m_{\bar{D}^{*0}}$  has led to speculation that the  $X(3872)$  may be the bound state of these two charged mesons. Other more exotic interpretations include a tetraquark (tightly bound state of four quarks) model, or charmonium-gluon hybrid bound states.

In order to identify what is the  $X(3872)$  state, experimentalists can make several attempts. First of all, determination of the quantum numbers such as spin ( $J$ ), parity ( $P$ ) and charge conjugation ( $C$ ) gives very important information. As already mentioned, the radiative decay of  $X(3872)$  to  $J/\psi\gamma$  final state determines  $C = +1$  ( $C$ -even) [8, 9]. The  $J/\psi\pi^+\pi^-$  mode enables us to assess other quantum numbers by the angular distribution analysis of the decay products. According to the Belle [26] and CDF [27] studies, still allowed quantum number assignments are  $J^{PC} = 1^{++}$  or  $2^{-+}$ . A next generation higher statistics experiment is necessary to identify one of these two. Second approach is search for the hypothesis-oriented decay mode. Motivated by the assumption that  $X(3872)$  is a  $D^0\bar{D}^{*0}$  molecule,  $B \rightarrow D^0\bar{D}^{*0}K$  modes are reconstructed and  $X(3872) \rightarrow D^0\bar{D}^{*0}$  has been confirmed. This decay mode's branching fraction is found to be approximately 10 times larger than  $J/\psi\pi^+\pi^-$  mode [28].

This result seems to support the interpretation as a molecular state, however there are several unsolved question assuming that it has  $J^{PC} = 1^{++}$ . Difference between the observed mass and  $D^0\bar{D}^{*0}$  threshold is representing the binding energy and it is found to be small,  $0.1 \pm 0.35 \text{ MeV}$ . This binding energy can be translated into the distance between  $D^0$  and  $\bar{D}^{*0}$  under the Yukawa-type potential with pion exchange. That distance corresponds to the size of  $X(3872)$  and is found to be about 5 fm, comparable spacial spreading with the lead nuclei [29]. On the other hand, the size of  $J/\psi$  meson is about 0.4 fm, therefore volume difference is so large,  $\mathcal{O}(10^3)$ , that the probability for  $c$  and  $\bar{c}$  quarks to meet each other to form  $J/\psi$  can not be one tenth but should be much smaller, then contradicting with the observed facts. In addition, such very loosely bound object can hardly be produced by the high energy  $p\bar{p}$  collisions at Tevatron, thus it would not be easy to explain the  $X(3872)$  production cross section measured by CDF experiment [30].

Under such situation, search for the partner states of  $X(3872)$  will give us independent information to test interpretation of it. So far, though the search for  $X(3872)$ 's charged partner in  $J/\psi\pi^\pm\pi^0$  gave negative results [26, 31], the charged partner might be so broad that we can not get a proper signature in the current statistics and the  $X(3872)$ 's  $C$ -odd partner state can have moderately narrow decay width and may decay into the  $J/\psi\eta$  final state in a tetraquark model [32]. In more general argument, the  $C$ -odd partner can exist in either molecule or tetraquark pictures and the photon energy in  $\eta \rightarrow \gamma\gamma$  is well above the energy threshold to be detected in  $B$ -factories even in the case such resonance is just above  $J/\psi\eta$  mass threshold. Thus the  $J/\psi\eta$  system in the three-body  $B \rightarrow J/\psi\eta K$  decay is an important subject to discuss about the missing  $C$ -odd  $X(3872)$  partner.

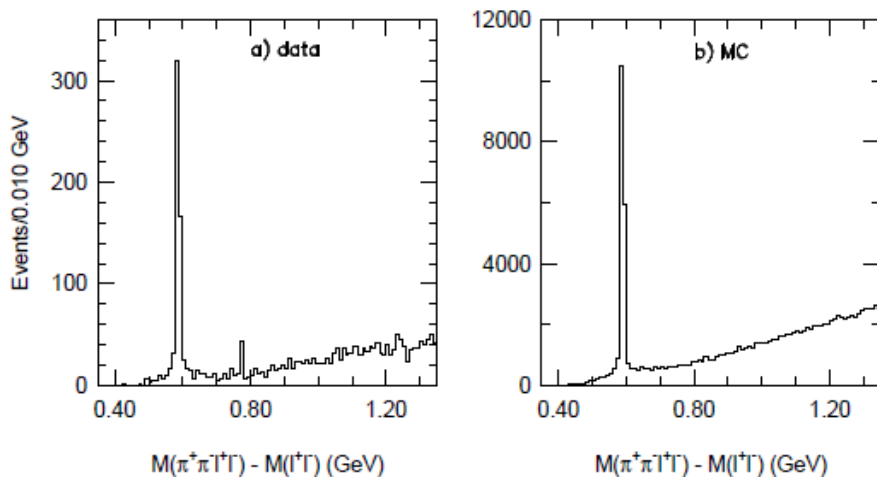


Figure 1.2: Observation of  $X(3872)$ . In (a), narrow peak around  $3.872 \text{ GeV}/c^2$ .



# Chapter 2

## The Belle experiment

The Belle experiment is one of two dedicated  $B$  physics experiments in the world and it is located the High Energy Accelerator Research Organization (KEK), Tsukuba, Japan. Another  $B$ -factory experiment, BaBar is performed at the Stanford Linear Accelerator Center (SLAC), California, USA. The  $B$ -factory at KEK consists of two separate entities, the KEKB  $e^+e^-$  collider and the Belle detector.

### 2.1 The KEKB accelerator

The KEKB accelerator [23], which was commissioned in December 1998, is designed to produce large number of  $B\bar{B}$  pairs by colliding electrons and positrons of asymmetric energy. It consists of two storage rings, an 8 GeV electron high energy ring (HER) and a 3.5 GeV positron low energy ring (LER). The two storage rings are located side by side in the accelerator tunnel originally built for the TRISTAN  $e^+e^-$  collider project. The accelerator is located 11 m underground and have a circumference of roughly 3 km. There is only one beam crossing point where the  $e^+e^-$  collision takes place, known as the interaction point (IP). A linear accelerator (Linac) accelerates the electrons and positrons to their required energies and inject them into their respective storage rings. Figure 2.1 shows a schematic of the KEKB collider. Electrons and positrons are kept in bunches around the storage rings. There are approximately 1000 bunches in each ring which corresponds to a bunch separation of around 3.0 m. The electrons and positrons collide with a finite crossing angle of  $\pm 11$  mrad to avoid the parasitic interactions of bunches

near but not at the IP.

The centre-of-mass energy at the collision point is nominally  $\sqrt{s} = 10.58$  GeV, which coincides with the peak of the cross section to produce the  $\Upsilon(4S)$  resonance. This is the optimized choice to get  $B$  meson data as much as possible because the  $\Upsilon(4S)$  decays to a  $B\bar{B}$  pair more than 96%. The mass of the  $B$  meson is almost half the  $\Upsilon(4S)$  mass, thus it will be produced roughly at rest in the  $\Upsilon(4S)$  rest frame.

The advantage of the asymmetric collider is that the  $B$  mesons receive a Lorentz boost,  $\beta\gamma = 0.425$ , in the laboratory frame along the direction of the beam line ( $z$  coordinate), thus simplifying the kinematics of the  $B\bar{B}$  pair to one-dimension. The boost also gives the  $B$  mesons a mean flight length of about  $200 \mu\text{m}$  in the laboratory frame making it feasible with current technology to measure a separation between the decay points of the  $B\bar{B}$  pair in  $z$  direction,  $\Delta z$ . This allows the time difference between two  $B$  meson decays to be calculated as  $\Delta t \simeq \Delta z / \beta\gamma c$ . It is an indispensable feature of the experimental apparatus to realize time-dependent  $CP$  violation measurement in  $B$  meson system.

The KEKB collider and the Belle detector were operated not only on the  $\Upsilon(4S)$  resonance but also on  $\Upsilon(1S)$ ,  $\Upsilon(2S)$ ,  $\Upsilon(3S)$  and  $\Upsilon(5S)$  as well as 60 MeV below  $\Upsilon(4S)$  for understanding of continuum background. The design luminosity of the KEKB collider was  $\mathcal{L} = 1.0 \times 10^{34} \text{ cm}^{-2}\text{s}^{-1}$ , which corresponds to an approximate production rate of 10  $B\bar{B}$  pairs per second. By the completion of the operation at 2010, we have well exceeded this design luminosity with the world record of  $\mathcal{L} = 2.11 \times 10^{34} \text{ cm}^{-2}\text{s}^{-1}$ , and our accumulated luminosity is now greater than  $1000 \text{ fb}^{-1}$ . Out of those, an integrated luminosity of  $703 \text{ fb}^{-1}$  was recorded at  $\Upsilon(4S)$ . The number of  $B\bar{B}$  pairs recorded in that data sample is  $772 \times 10^6$ .

## 2.2 The Belle detector

The Belle detector is a large solid-angle magnetic spectrometer that can detect the following final state particles ( $K^\pm, \pi^\pm, e^\pm, \mu^\pm, p(\bar{p}), \gamma$  and  $K_L^0$ ). Since a  $B$  meson will eventually decay to some combination of these final state particles most of the time, it is important that these particles can be detected and identified with high efficiency. The Belle detector was designed to achieve this task with many sub-detectors as shown in Fig 2.2, and is placed asymmetrically around the IP because of the direction of the boost. The following

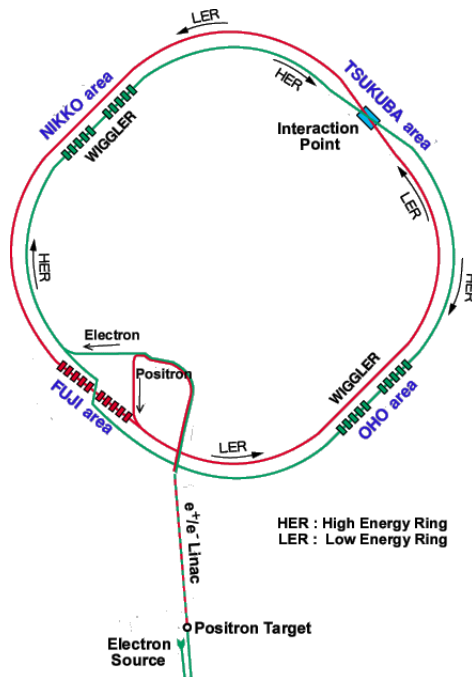


Figure 2.1: The KEKB collider.

sections describe the various sub-detectors and further details can be found in Ref. [24].

Now we describe the Belle coordinate systems used in this thesis. In Cartesian coordinates,  $z$  is defined as being the direction opposite the positron beam line,  $y$  is vertically upwards, and  $x$  is in the direction of the cross product,  $x = y \times z$ . Cylindrical coordinates are also used. The radius,  $r = \sqrt{x^2 + y^2}$ , is defined in the  $x$ - $y$  plane,  $\theta$  is the polar angle from the  $z$ -axis, and  $\phi$  is the azimuthal angle around the  $z$ -axis. Further details of the hardware components are to be described.

### 2.2.1 Beampipe

Although not active component of the Belle detector, the beampipe around the IP is the first piece of material through which particles must traverse before reaching the detector. Since Coulomb scattering affects track resolution, it is important to minimise the impact of the beampipe on particle

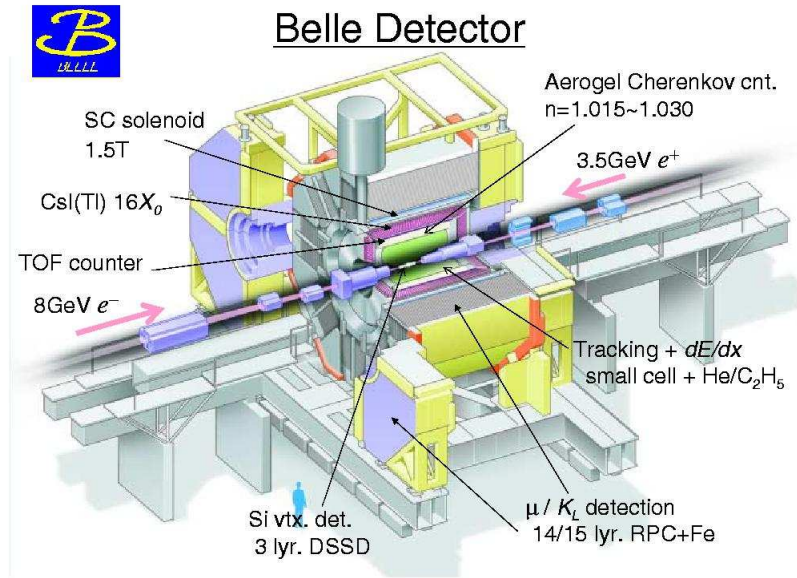


Figure 2.2: Cut-away view of the Belle detector.

trajectories by choosing a thin material with low atomic number. In addition, track quality is reduced as the detector is further removed from the IP. So the diameter of the beampipe must also be as small as possible.

With these considerations in mind, a beryllium beampipe was chosen. The beampipe is a dual layer cylinder whose radii are 20.0 mm and 23.0 mm respectively, where each cylinder has a 0.5 mm thickness. The 2.5 mm gap between the cylinders is used as a helium gas channel which acts as a coolant. This prevents overheating induced by the beam and minimally interferes with tracks due to its low atomic number. The outer layer is covered with a 20  $\mu\text{m}$  thick gold sheet to reduce low energy X-ray background from the HER. The total thickness of the beampipe corresponds to 0.9% of a radiation length.

After the first  $152 \times 10^6$   $B\bar{B}$  pairs were accumulated, the innermost detector was redesigned to accommodate new 4-layer SVD having an improved acceptance and to get closer to the IP. The radius of the inner cylinder of the new beampipe is now 15.0 mm. Fig 2.3 shows the design of the original beampipe. The new beampipe has almost same structure except for the radius and newly

introduced paraffin coolant.

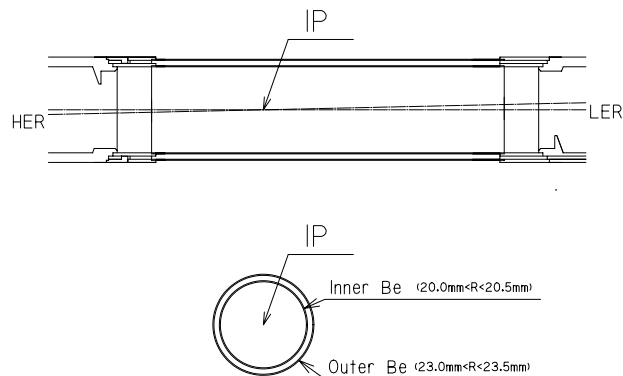


Figure 2.3: Side view and cross section of the beampipe used for accumulation the first  $152 \times 10^6$   $B\bar{B}$  pairs.

### 2.2.2 Silicon Vertex Detector (SVD)

The Silicon Vertex Detector is the most important detector in the time-dependent  $CP$  analysis as it is responsible for precise measurement of  $B$  vertex positions. This is achieved via the high spatial resolution of the SVD. The SVD is the innermost detector and consists of three concentric cylindrical layers of silicon sensors which cover the polar angle,  $23^\circ < \theta < 139^\circ$ . This corresponds to 86% of the solid angle. The radii of the innermost, middle, and outermost layers are 30.0, 45.5 and 60.5 mm, consisting of 8, 10 and 14 ladders, respectively. Each ladder is made up of two half-ladders that are joined by a support structure but are electrically independent of each other. A long half-ladder contains two double sided silicon strip detectors (DSSD) and a hybrid unit which processes signals from the DSSD. A short half-ladder contains a DSSD and a hybrid unit. The innermost layer consists of two short half-ladders, the middle layer consists of a short and long half-ladder and the outermost-layer ladder consists of two long half-ladders.

The DSSD, manufactured by Hamamatsu Photonics, was originally developed for the DELPHI detector [25]. Its dimensions are  $57.5 \times 33.5$  mm<sup>2</sup> with a thickness of 300  $\mu$ m. Each DSSD consists of 1280 sense strips and 640

readout pads on both sides. One side of the DSSD ( $n$ -side) has its  $n^+$  sense strips, each separated by  $42\ \mu\text{m}$ , oriented perpendicular to the beam direction to measure the  $z$  coordinate. The  $p^+$  sense strips, each separated by  $25\ \mu\text{m}$ , on the other side ( $p$ -side) are oriented longitudinally which allows the  $r$ - $\phi$  position to be measured. A DSSD is basically a  $pn$  junction. A bias of  $75\text{V}$  is supplied to the  $n$ -side, while the  $p$ -side is grounded. The  $n^+$  strips are interleaved by  $p^+$  implants ( $p$ -stops) to electrically separate the consecutive strips. A charged particle passing through the  $n$  bulk silicon creates electron-hole pairs. The electrons and holes drift to their corresponding biased side of the DSSD making a 2-dimensional hit signal. On the  $n$ -side, adjacent strips are read out by a single channel, giving an effective strip separation of  $84\ \mu\text{m}$ . On the  $p$ -side, every other strip is connected to a readout channel. Charge collected by the floating strips in between is read from adjacent strips by capacitive charge division. A schematic of the DSSD is shown in Fig 2.4.

A redesigned SVD was installed after  $152 \times 10^6\ B\bar{B}$  pairs were accumulated. The SVD already described is called SVD1 and was replaced with the 4-layer SVD2. Among the several improvements were that the angular acceptance of SVD2 was increased to  $17^\circ < \theta < 150^\circ$ , and the innermost layer was moved  $1.0\ \text{cm}$  closer to the IP to a radius of  $2.0\ \text{cm}$ . The fourth layer is accommodated by redesigning the inner region of the CDC. Fig 2.5 shows the geometry of the SVD. We estimate the performance of the SVD with two quantities. One is the SVD-CDC track matching efficiency which is defined as the probability that a CDC track passing through the SVD acceptance has associated SVD hits in at least two layers, and at least one 2-D hit. The CDC is the next innermost detector after the SVD and will be described later. The average matching efficiency is better than  $98.7\%$ .

### 2.2.3 Central Drift Chamber (CDC)

The Central Drift Chamber is a charged particle tracking system that measures track momenta from their curvature in the magnetic field induced by the solenoid magnet. The CDC also measures  $dE/dx$  of charged tracks to provide particle identification information. A charged particle moving through a constant magnetic field will follow the path of a helix which is defined by five parameters. The first is the curvature of the helix which gives the transverse momentum,  $p_T$ , and the second gives the pitch which is related to the longitudinal momentum,  $p_L$ . The other three give the impact parameters. The inner side of the CDC is not encased with aluminium like the outer

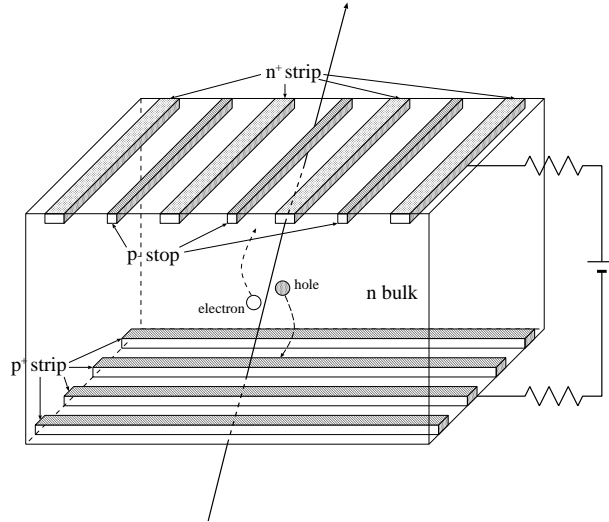


Figure 2.4: DSSD schematic.

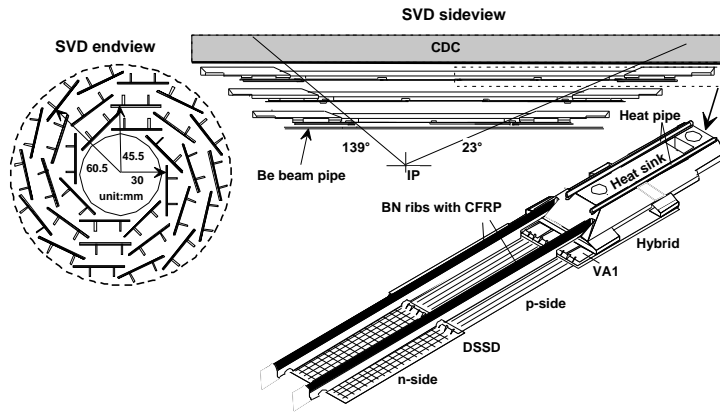


Figure 2.5: The schematic shows the SVD1 geometry.

parameters with respect to the IP. By minimising the amount of passive material in the way, good tracking efficiency can be maintained even for low  $p_T$  tracks. The CDC coverage is  $17^\circ < \theta < 150^\circ$  which corresponds to 92%

of the solid-angle. Figure 2.6 shows the geometry of the CDC. The CDC is filled with a gas consisting of 50% helium and 50% ethane. The low-Z gas mixture is useful for minimising multiple Coulomb scattering to ensure a good momentum resolution, especially for low momentum tracks. The CDC contains a total of 8400 drift cells. A drift cell is made up of eight grounded wires providing an electric field which surrounds a positively biased sense wire. The CDC cell structure is shown in Fig 2.7.

When a charged particle passes through a drift cell, electrons are dislodged from the gas and drift towards the sense wire. In the final 1 mm, the electric field increases as  $1/r$ . This accelerates the electrons sufficiently to cause secondary ionisation which, in turn, cause further ionisation resulting in a cascade of charge. This process, called gas amplification, increases the signal by a factor a few  $10^4$ . Before amplification, the electrons have a specific drift velocity, so the measured pulse height and drift time are related to the energy deposit,  $dE/dx$ , and distance from the sense wire. Roughly half the wires are oriented parallel to the  $z$ -direction (axial) to provide  $p_T$  information while the remaining wires are oriented at a small angle,  $\pm 50$  mrad, to the  $z$ -direction (stereo) to give  $p_L$ . Figure 2.8 shows a scatter plot of the measured  $dE/dx$  as a function of the particle momentum. Separation between pions, kaons, protons and electrons can clearly be seen with particle momenta below 1 GeV/ $c$ . Now that the behaviour of particles with different mass have shown distinct characteristics in  $dE/dx$ , we can perform particle identification on an unknown track that traverses the CDC.

#### 2.2.4 Aerogel Cerenkov Counter (ACC)

The role of the Aerogel Cerenkov Counter is to provide particle identification information to distinguish charged kaons from charged pions in the momentum range of 1.0 to 4.0 GeV/ $c$ . Cerenkov radiation is emitted when the velocity of a charged particle in a medium exceeds the speed of light in the same medium,

$$n > \frac{1}{\beta} = \sqrt{1 + \left(\frac{m}{p}\right)^2} \quad (2.1)$$

where  $m$  and  $p$  are the mass and momentum of the particle, and  $n$  is the refractive index of the material. Therefore, we can distinguish kaons from pions, muons and electrons by selecting a material in which pions emit Cerenkov light, but heavier kaons do not.

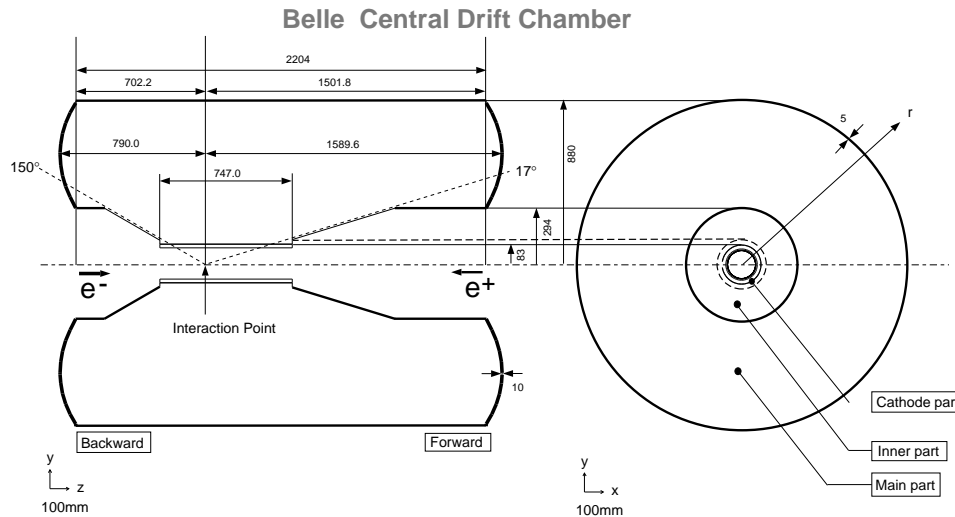


Figure 2.6: CDC geometry.

The ACC can be divided into two regions, the barrel and the forward endcap. The barrel consists of 960 counter modules separated into sets of 60 in the  $\phi$  direction. There are 228 modules that occupy the forward endcap in 5 concentric layers. Each counter is arranged in the way to points towards the direction of the IP. Fig 2.9 and 2.10 show the geometry of the ACC and ACC modules of barrel part and endcap part.

A counter module consists of silica aerogel blocks encased in an aluminium box of roughly  $12 \times 12 \times 12 \text{ cm}^3$  in size. One or two photomultiplier tubes capable of operating in the 1.5 T magnetic field are attached to the sides of each box to detect Cerenkov photons. The refractive indices of the silica aerogel blocks are selected to maintain good kaon/pion separation over the kinematic range stated earlier. For the barrel modules, silica aerogel with five different refractive indices,  $n = 1.010, 1.013, 1.015, 1.020$  and  $1.028$  are used depending on the polar angle. Silica aerogel with  $n = 1.030$  is used in the forward endcap modules, to encompass lower momentum particles. This is because the TOF, designed for particle identification with low momentum particles and the next sub-detector in line, is not present in the endcap.

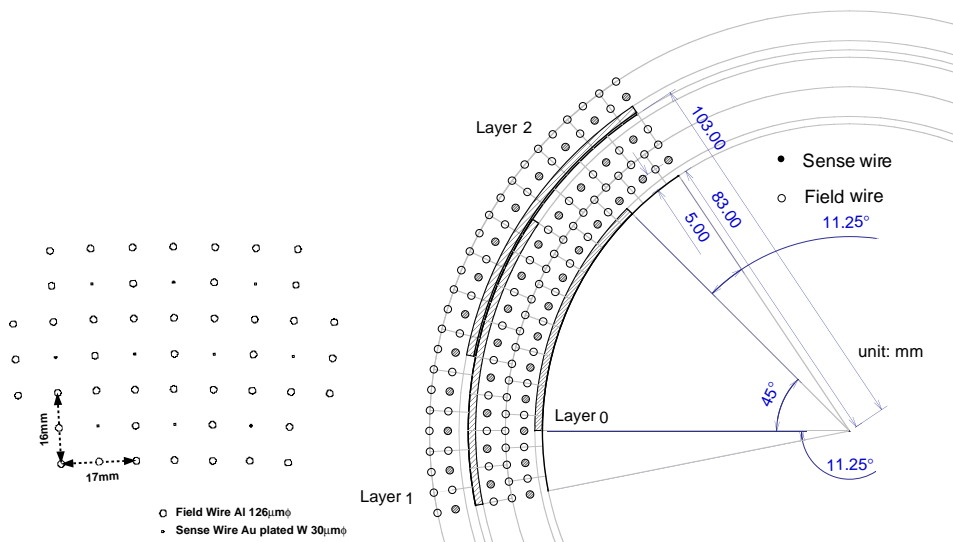


Figure 2.7: CDC cell structure.

### 2.2.5 Time of Flight Counter (TOF)

The Time of Flight Counter gives particle identification information to distinguish charged kaons from pions in the low momentum region, below 1.2 GeV/c. The particle mass ( $m$ ), can be determined from its relation to the measured elapsed time from collision at the IP, and is expressed as,

$$T = \frac{L}{c\beta} = \frac{L}{c} \sqrt{1 + \left(\frac{m}{p}\right)^2} \quad (2.2)$$

where  $p$  is the momentum of the track and  $L$  is the flight length. The TOF sub-detector consists of plastic scintillation counters attached to the fine-mesh type photomultiplier tubes and has a timing resolution of 100 ps. The TOF also provides fast timing signals for the data acquisition and the trigger system. To sustain a fast trigger rate in any beam background condition, thin trigger scintillation counters (TSC) are placed just before the TOF counter. A TOF module consists of two TOF counters and one TSC counter, a schematic of which is shown in Fig 2.11.

In total, there are 64 TOF modules located in the barrel region at a radius

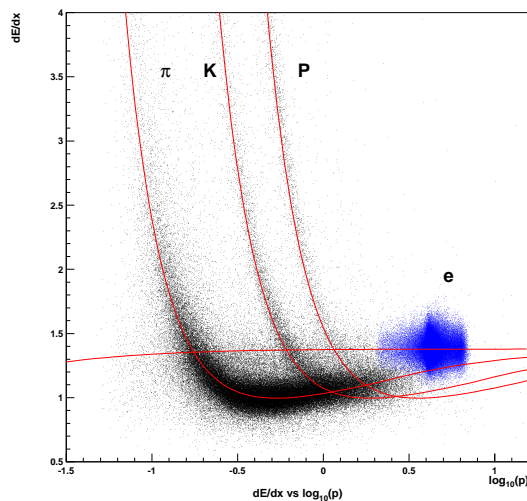


Figure 2.8:  $dE/dx$  vs momentum taken from collision data.

of 1.2 m from the IP, covering a polar angle of  $34^\circ < \theta < 120^\circ$ . Figure 2.12 shows the mass distribution obtained from TOF measurements. The data points are consistent with the simulation that assumes a time resolution of 100 ps.

### 2.2.6 Electromagnetic Calorimeter (ECL)

The Electromagnetic Calorimeter serves to identify electrons and photons by measuring electromagnetic showers. Electrons in this analysis are required for  $J/\psi$  reconstruction while photons are needed for the reconstruction of  $\eta$ . The ECL consists of 8736 thallium-doped CsI crystal (CsI(Tl)) counters. The CsI(Tl) crystal has a tower shape and is 30 cm long, which corresponds to 16.2 radiation lengths. Each CsI(Tl) crystal is arranged so that it points towards the IP. The barrel component has 6624 crystals divided into 46 in  $\theta$  and 144 in  $\phi$ . The forward (backward) endcap has 1152 (960) crystals divided into 13 (10) in  $\theta$  and 48- 144 (6-1 144)  $i\phi$  depending on  $\theta$ . The geometry of the ECL is shown in Fig 2.13.

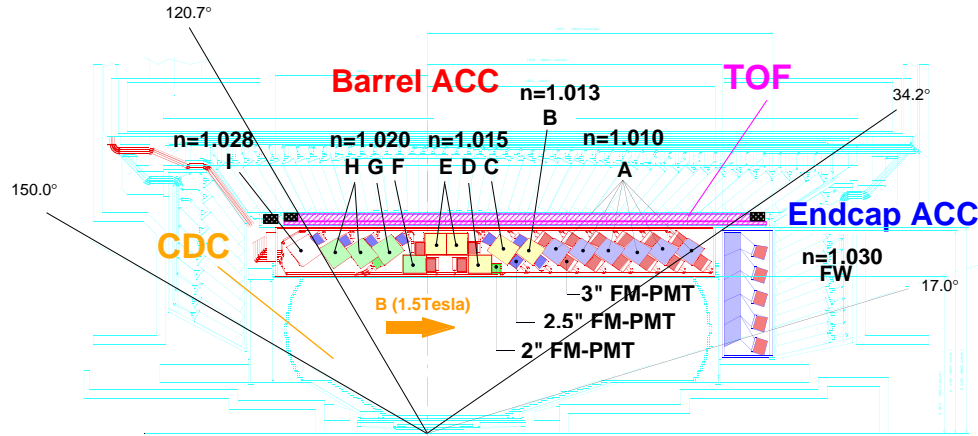


Figure 2.9: ACC geometry.

When an electron or photon hits a crystal, most of its energy is deposited in electromagnetic showers produced by bremsstrahlung and pair production. Other charged particles deposit a small amount of energy by ionisation. Therefore, the ratio of the cluster energy measured by the ECL to the momentum of the charged track momentum as measured by the CDC,  $E/p$ , is close to unity for electrons and lower for other particles. In this way, electron identification can be performed. The energy resolution of the ECL is given by

$$\frac{\sigma_E}{E} = (1.34 \oplus \frac{0.066}{E} \oplus \frac{0.81}{E^{1/4}})\% \quad (2.3)$$

where, E in GeV.

### 2.2.7 Solenoid Magnet

The superconducting solenoid provides a magnetic field of 1.5 T, that bends charged particles in a helix to enable track momentum measurement in the CDC. The superconducting coil consists of a single layer niobium-titanium-copper alloy embedded in a high purity aluminium stabiliser. The coil is

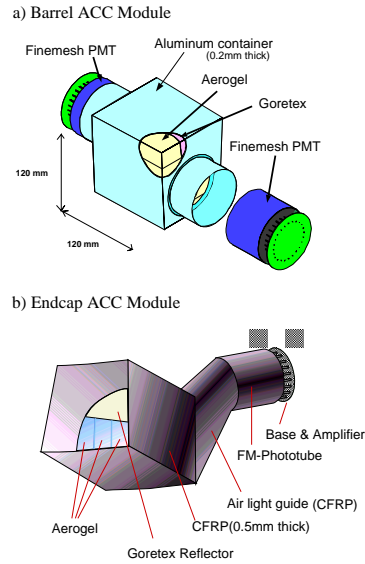


Figure 2.10: ACC modules. The top is barrel part module, bottom is endcap part module.

wound around the inner surface of an aluminium support cylinder of 3.4 m in diameter and 4.4 m in length. Cooling is provided by circulating liquid helium through a tube on the inner surface of the aluminium cylinder.

### 2.2.8 $K_L^0$ and Muon Detector (KLM)

The  $K_L^0$  and muon detector (KLM) provides muon identification for charged particles with enough momentum to reach the KLM,  $P_T > 0.6 \text{ GeV}/c$ . It can also detect the neutral  $K_L^0$ . Since these are highly penetrative particles, a lot of material is needed to identify them efficiently.

The KLM consists of alternating layers of charged particle detectors and 4.7 cm thick iron plates. There are 15 resistive plate counter (RPC) superlayers and 14 iron layers in the barrel region and 14 RPC superlayers in each endcap, covering the polar region,  $20^\circ < \theta < 155^\circ$ . The iron layers also serve as a return yoke for the magnetic flux provided by the superconducting solenoid. The KLM barrel part of the iron yoke is shown in Figure 2.14. Each RPC

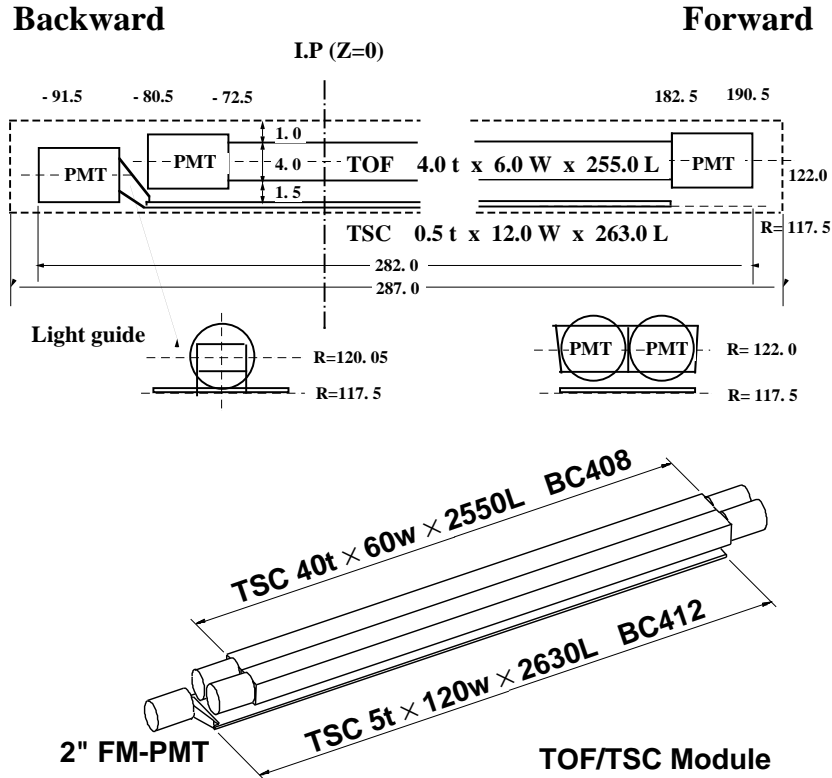


Figure 2.11: TOF module geometry.

superlayer consists of two RPC modules to provide 2-dimensional  $\theta$ - $\phi$  information. The cross section of an RPC superlayer is shown in Figure 2.15. Hadrons interacting with the iron plates produce a shower of ionising particles that are detected by the RPC layers. The result is a cluster of hits deposited in the KLM. A  $K_L^0$  candidate can be distinguished from another charged hadron because it will not leave an associated track in the CDC. A muon, on the other hand, does leave a charged track in the CDC. However, muons can still be distinguished from charged and neutral hadrons because they do not feel the strong interaction. Hadrons are more rapidly absorbed and deflected by strong interactions with iron resulting in wide clusters and

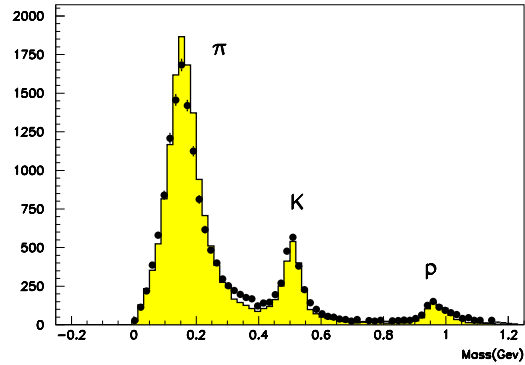


Figure 2.12: Mass distribution from TOF measurements for particle momenta below  $1.2\text{GeV}/c$ .

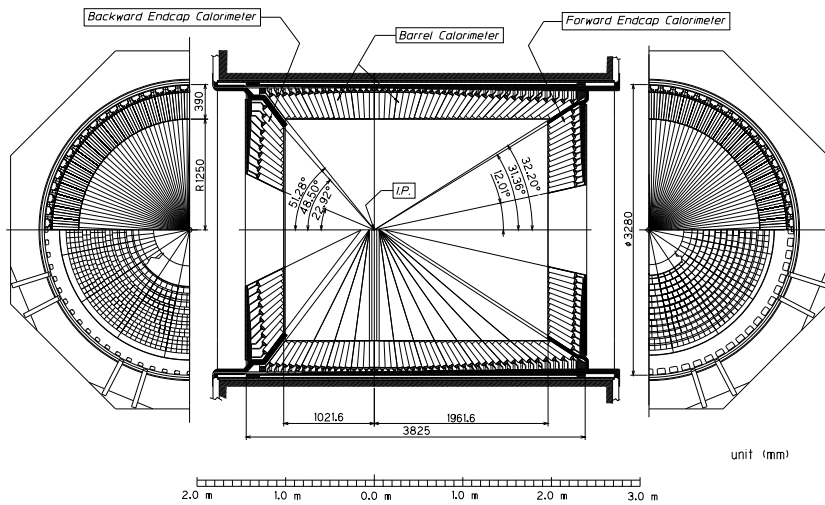


Figure 2.13: ECL geometry.

are stopped within a few layers of iron. Muons only experience electromagnetic multiple scattering and energy loss, so their clusters tend to be thinner and they have far greater penetration depth.

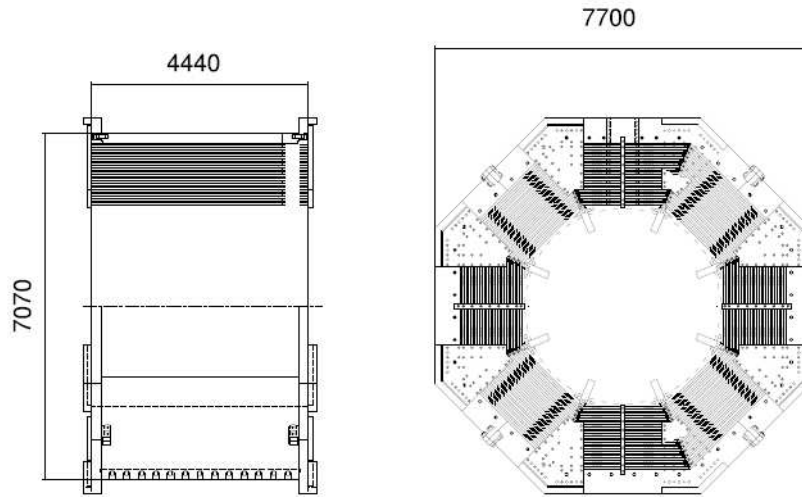


Figure 2.14: KLM geometry in units of mm.

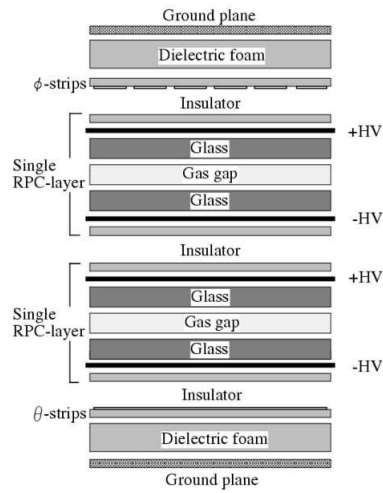


Figure 2.15: Cross section of an RPC superlayer.

## 2.2.9 Trigger and Data Acquisition

The role of the trigger system is to distinguish and record the interesting physics events from the enormous amount of background that enters the de-

tector, using fast signals from the sub-detectors. Because of the high beam current of the KEKB accelerator, the trigger suffers severe beam background, and since the rates of beam background are very sensitive to real-time accelerator conditions, it is difficult to estimate reliably. For this reason, the trigger system is required to be flexible so that background rates can be kept within the tolerance of the data acquisition system. Redundant triggers are also needed to keep the high trigger efficiency for interesting physics events. The Belle trigger system consists of the Level-1 hardware trigger and the Level-3 software trigger which operate in real-time. The Level-4 trigger and event reconstruction and classification is performed offline. A flow diagram of the Belle trigger system is shown in Figure 2.16.

The Level-1 trigger consists of the sub-detector trigger systems and the central trigger system called the Global Decision Logic (GDL). The sub-detector trigger systems are categorised into two: track triggers and energy triggers. The CDC and TOF are responsible for charged track trigger signals while the ECL provides triggers based on the total energy deposit. The KLM provides additional trigger signals for muons. A schematic of the Belle Level-1 trigger system is shown in Figure 2.17. These are four main sub-triggers in the GDL, the two track trigger, the three track trigger, the cluster number trigger and the energy sum trigger. The two track trigger requires twotracks with an opening angle greater than  $135^\circ$ . At least one track must have  $z$  information and a minimum of 2 hits in the TOF. The three track trigger is similar to the two track trigger, but no opening angle condition is required. At least three hits in the inner tracking sub-detectors are required. The cluster number trigger requires at least 4 isolated clusters in the ECL. The energy sum trigger requires at least 1 GeV of energy deposited in the ECL.

The GDL combines the sub-detector trigger signals and makes the final decision to initiate a Belle-wide data acquisition (DAQ) within  $2.2 \mu\text{s}$  of the beam crossing. The typical trigger rate is 200-250 Hz. With redundant triggers in place, the trigger efficiency for  $B\bar{B}$  events is greater than 99.5%.

The performance goal of the DAQ is to be operational at a maximum trigger rate of 500 Hz, while keeping the dead time fraction to less than 10%. In order to achieve this, the entire DAQ system is divided into seven sub-systems running in parallel. An event builder combines the signals from sub-detectors into a single event and passes it to an online computer farm. The online computer performs a basic track and cluster reconstruction and further rejects unwanted events with the Level-3 trigger. The remaining events are sent to a computer centre for offline processing. A schematic of the Belle DAQ system

is shown in Figure 2.18.

The Level-4 trigger is applied first during offline processing. Events must have at least one track originating from the IP,  $dr < 1.0$  cm and  $|dz| < 4.0$  cm, with  $p_T > 300$  MeV/ $c$ . Events passing the Level-4 trigger undergo full event reconstruction. Tracks are reconstructed with hits in the CDC, then these tracks are extrapolated towards the IP to search for associated SVD hits. They are also extrapolated outwards to search for hits in the outer detectors. Thus, 4-vectors and particle identification likelihoods can be assigned. Clusters in the ECL are also reconstructed to form photons. This information along with many other calculated variables are stored in a format available to collaborators for analysis.

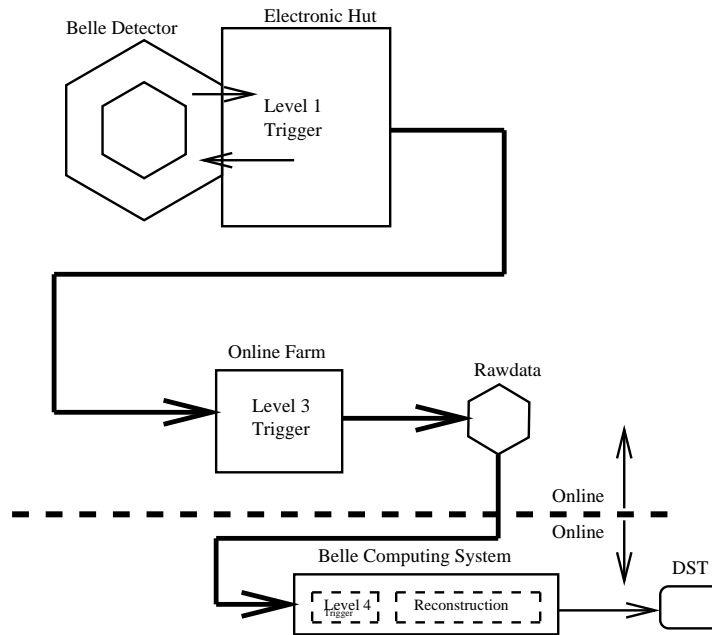


Figure 2.16: An overview of the Belle trigger system.

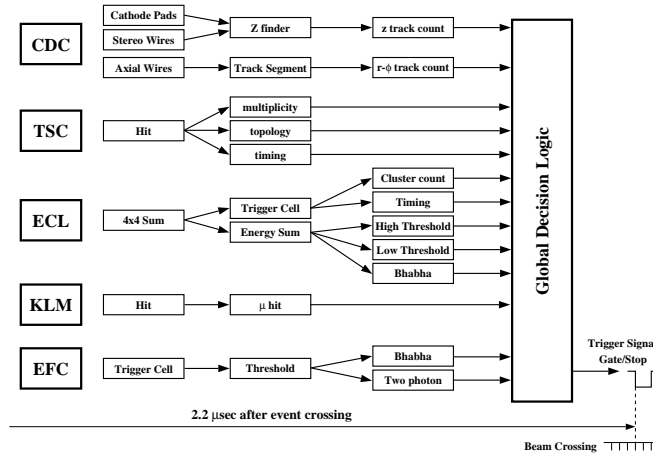


Figure 2.17: The Belle Level-1 trigger system.

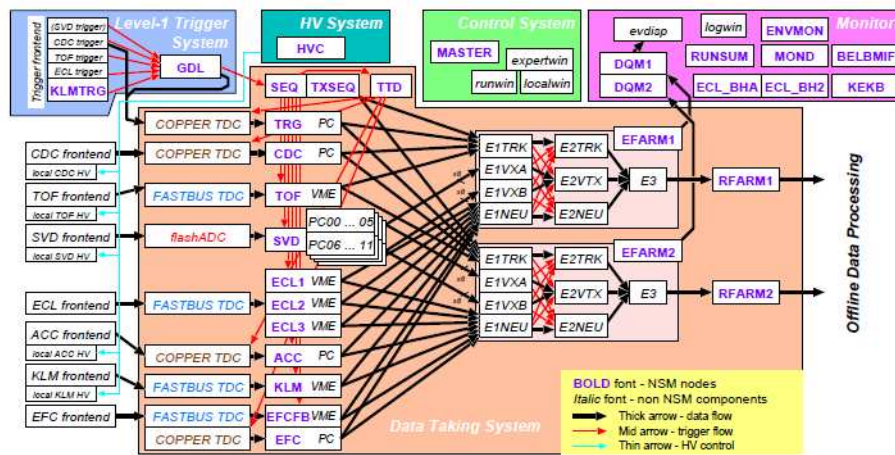


Figure 2.18: The Belle DAQ system.



# Chapter 3

## Event selection for $B \rightarrow J/\psi\eta K$ decays

The target  $B$  meson decay modes,  $B^\pm \rightarrow J/\psi\eta K^\pm$  and  $B^0 \rightarrow J/\psi\eta K_S^0$  are reconstructed by combining these daughter particle candidates,  $J/\psi$ ,  $\eta$  and  $K^\pm$  or  $K_S^0$  mesons.  $K^\pm$  is stable but all other daughters are unstable, therefore we need to reconstruct them by the proper final states for each. The analysis procedure to carry out that task is described in this chapter.

### 3.1 Data sample

After the first physics run in 1999, Belle experiment accumulated  $e^+e^-$  beam collision data mostly on the  $\Upsilon(4S)$  resonance. Operation of KEKB accelerator and Belle detector at that energy continued until 2008. In total an integrated luminosity of  $703 \text{ fb}^{-1}$  are recorded and there are  $772 \times 10^6$   $B\bar{B}$  pairs in this high statistics data sample. It is the basis of this work.

In order to understand acceptance and performance of the detector to estimate detection efficiency for  $B \rightarrow J/\psi\eta K$  decay signal and possible background contamination, an appropriate Monte Carlo simulation (MC) has to be used. In order to generate  $B \rightarrow J/\psi\eta K$  decay signal events as well as probable background events, the EvtGen program [33] is used. This program is capable to treat the key kinematics and resultant decay products angular distributions, not only distributing according to the available phase space but also isotropic angular distribution in the  $B$  meson decays into two pseudoscalar mesons, or the final state becomes linear combination of relative

angular momentum of  $S$ -,  $P$ - and  $D$ -waves in the case into two vector mesons for example. This software can also handle the time-dependent  $CP$  violation in the neutral  $B$  meson decays into a  $CP$  eigenstate. For the description and modeling of the detector material and particles' interaction during their passage, the GEANT3 [34] software is used. Based on the particle's energy loss in the active material, the detector response including the readout electronics as well as digitization effect is simulated by the hand-made codes composed by Belle collaborators.

In order to estimate reconstruction efficiencies for  $B^\pm \rightarrow J/\psi\eta K^\pm$  and  $B^0 \rightarrow J/\psi\eta K_S^0$  modes,  $5 \times 10^5$  events for each are generated with the three-body distribution obeying the available phase space, sometimes denoted as PHSP hereafter.  $B^\pm \rightarrow \psi' K^\pm$  and  $B^0 \rightarrow \psi' K_S^0$  are well established decay modes and these can be a part of signal when  $\psi' \rightarrow J/\psi\eta$  decay occurs. Therefore these  $B$  decay modes are also simulated up to the same amount as the PHSP using the corresponding chain of two-body decays. In this study, main backgrounds come from  $B\bar{B}$  events in which one of the  $B$  decays to the final state containing a real  $J/\psi \rightarrow e^+e^-$  or  $\mu^+\mu^-$ , i.e. the  $B \rightarrow J/\psi X$  processes. In order for understanding of these backgrounds, a large amount of MC simulation sample for the  $B \rightarrow J/\psi X$  is prepared by including the most up-to-date  $B$  meson decay modes information as of 2010 April. We call this MC sample as the inclusive  $J/\psi$  MC throughout this thesis.

## 3.2 Reconstruction and identification of particles

At first, charged particle reconstruction in CDC with SVD and shower reconstruction in ECL are done. After those, more detailed information is necessary to be obtained to pick up the  $B$  decay daughter particles in the final state correctly as much as possible. Among the daughter particles coming from the target  $B$  decays, lepton identification and photon detection are necessary to reconstruct  $J/\psi \rightarrow e^+e^-$  or  $\mu^+\mu^-$  and  $\eta \rightarrow \gamma\gamma$  decays. Selection procedures for charged and neutral Kaons are described later in the proper subsections.

### 3.2.1 Charged particle detection

The first step of charged particle reconstruction is finding track-segment-hit-patterns in the CDC. The tracks projected onto the  $r - \phi$  plane are searched for with axial wire hits, then hits of the stereo wires are used to determine  $z$  positions of the track. Track parameters (momentum and position) of the found track are obtained by the fitting based on the Kalman filter technique, which minimizes the effects of the multiple Coulomb scattering and non-uniformity of the magnetic field in the CDC in the determination of the track parameters. Then, all of the hit points are connected and fitted to a helix to obtain the particle momentum and position. Finally, the reconstructed tracks are connected to the SVD hits to improve the resolution of track parameters. Here, the track parameters are computed again with combination of the hits on the CDC and SVD.

### 3.2.2 Shower reconstruction and photon selection

The  $\gamma$  is a neutral particle, hence they can not be identified directly. In Belle detector, the  $\gamma$  candidate identification is based upon their electromagnetic interactions inside the ECL by a shower production mechanism of  $\gamma$ . In order to reconstruct showers, at first the seed crystals that have higher energy than surrounding crystals and exceeding 10 MeV are picked up. The  $5 \times 5$  crystal matrix centered at the seed crystal is looked for. The crystals' energy deposit more than the proper threshold, typically 0.5 MeV, are summed to obtain the incident particle energy. The incident position is estimated by the energy-weighted center of gravity of the included crystals' energies. Finite shower leakage effect and possible bias of the estimated incident position are corrected by the knowledge obtained by large statistics single- $\gamma$  MC event sample.

Reconstructed charged particle tracks are extrapolated to the ECL. The shower that does not have any associated charged track are recognized as  $\gamma$  candidate.

### 3.2.3 $B\bar{B}$ event selection

Electron-positron colliders operated at the  $\Upsilon(4S)$  resonance do not always produce  $B\bar{B}$  events. In fact, non- $B\bar{B}$  events have larger cross section and the most common are in the Bhabha reaction which is  $e^+e^-$  elastic scattering.

Also present are radiative Bhabha, other lepton pair production,  $e^+e^- \rightarrow l^+l^-$ , where  $l = \mu, \tau$ , two-photon events,  $e^+e^- \rightarrow \gamma\gamma$ , and beam-gas interactions. Non- $B\bar{B}$  hadronic events may also be produced and occur when,  $e^+e^- \rightarrow qq$  where  $q = u, d, s, c$  represent the light quarks and is known as continuum. Hadronic events including  $B\bar{B}$  pair production are selected if they satisfy the following criteria: at least three reconstructed charged tracks; a total reconstructed ECL energy in the center of mass (cms) frame in the range between  $0.1\sqrt{s}$  and  $0.8\sqrt{s}$ , where,  $\sqrt{s}$  is the total cms energy; an average ECL cluster energy below 1 GeV; at least one ECL shower in the region  $-0.7 < \cos\theta < 0.9$  in the laboratory frame; a total visible energy, exceeding  $0.2\sqrt{s}$ , and reconstructed primary vertex that is consistent with the known interaction point. After imposing these requirements, the efficiency for selecting  $B$  meson pairs that include a  $J/\psi$  meson is estimated by Monte Carlo (MC) simulation to be 99%.

### 3.2.4 $\mu, e$ identification

Muons are identified on the basis of track penetration depth and hit scatter pattern in the KLM system. These informations are arranged into a likelihood to be a muon,  $L_\mu$ . The track is identified as muon if the criteria of  $L_\mu > 0.1$  is satisfied. While, electrons are identified on the basis of electron likelihood  $L_e > 0.01$ , which uses  $dE/dx$  in CDC,  $E/p$  ratio ( $E$  is the energy deposited in the ECL and  $p$  is the momentum measured in CDC and SVD), shower shape in the ECL, distance between the experimented track and the reconstructed shower center and number of Cerenkov photon in the ACC.

### 3.2.5 Kinematic fit

Kinematic fitting reduces the effects of detector resolution to improve the mass or momentum resolutions and determine the decay vertex of a candidate particle. There are two types of kinematic fitting used in this analysis: mass-constrained fitting and vertex-constrained fitting. In the mass-constrained fitting, the invariant mass of the candidate,  $M_{\text{cand}}$ , is set to the known mass and the momentum of its daughters are re-calculated. This approach is applicable when the reconstructed state has narrow width and the observed invariant mass distribution is dominated by the detector resolution. The underlying motivation for vertex-constrained fitting is that the tracks used to reconstruct a candidate may not pass through the same point. The

$M_{\text{cand}}$  decay vertex is obtained by tuning the momentum and position of each daughter according to its measurement errors so that all tracks pass through a single point. These tuning of momentum or position are done by minimization of the  $\chi^2$  based on the involved particles momentum, position and their estimated errors. The minimization procedure is carried out by a Lagrange multiplier approach.

### 3.2.6 $J/\psi$ reconstruction

$J/\psi$  is reconstructed using its dileptonic decay,  $J/\psi \rightarrow \ell^+\ell^-$  where  $\ell$  corresponds to  $e$  or  $\mu$ . The branching fraction of  $J/\psi \rightarrow \ell^+\ell^-$  is  $(11.87 \pm 0.08) \times 10^{-2}$  (combine  $J/\psi \rightarrow e^+e^- : (5.94 \pm 0.06) \times 10^{-2}$  and  $J/\psi \rightarrow \mu^+\mu^- : (5.93 \pm 0.06) \times 10^{-2}$ ). Electron and muon pairs are selected from the charged tracks after applying electron likelihood ( $L_e$ ) larger than 0.01 and muon likelihood ( $L_\mu$ ) larger than 0.1, respectively. In order to include the bremsstrahlung photon emitted by either electron or positron,  $\gamma$ s within 50 mrad of the initial momentum are added, in order to reduce the lower side tail of invariant mass distribution. Figure 3.1 shows invariant mass of  $J/\psi$  of signal MC and data. As we can still miss some photons, we apply asymmetric cut on the invariant mass of  $M_{e^+e^-(\gamma)}$ ,  $-0.150 \text{ GeV}/c^2 < M_{e^+e^-(\gamma)} - M_{J/\psi} < 0.036 \text{ GeV}/c^2$ . For muon, invariant mass of  $M_{\mu\mu}$  is required to satisfy  $-0.06 \text{ GeV}/c^2 < M_{\mu\mu} - M_{J/\psi} < 0.036 \text{ GeV}/c^2$ . Here  $M_{J/\psi}$  mass denotes the nominal  $J/\psi$  mass and invariant mass requirements are indicated by the vertical red lines in Figure 3.1. Then, we used vertex fit and mass constraint fit to improve the momentum resolution for the reconstructed  $J/\psi$  candidates.

### 3.2.7 $\eta$ reconstruction

We use  $\eta \rightarrow \gamma\gamma$  decay to reconstruct  $\eta$  because it has the large branching fraction of  $(39.31 \pm 0.20) \times 10^{-2}$ . In order to reduce the background coming from low energy  $\gamma$ s, we require of  $E_\gamma > 100 \text{ MeV}$  where  $E_\gamma$  is the reconstructed photon energy. Also, the photon pair having large energy asymmetry is rejected using energy balance  $A_E$ , that is defined as follows

$$A_E = \frac{|E_1 - E_2|}{E_1 + E_2} \quad (3.1)$$

where,  $E_1(E_2)$  is the energy of  $\gamma_1(\gamma_2)$ , to reduce combinational background. We require  $A_E < 0.8$ . To remove the background coming from  $\pi^0$ s, if a

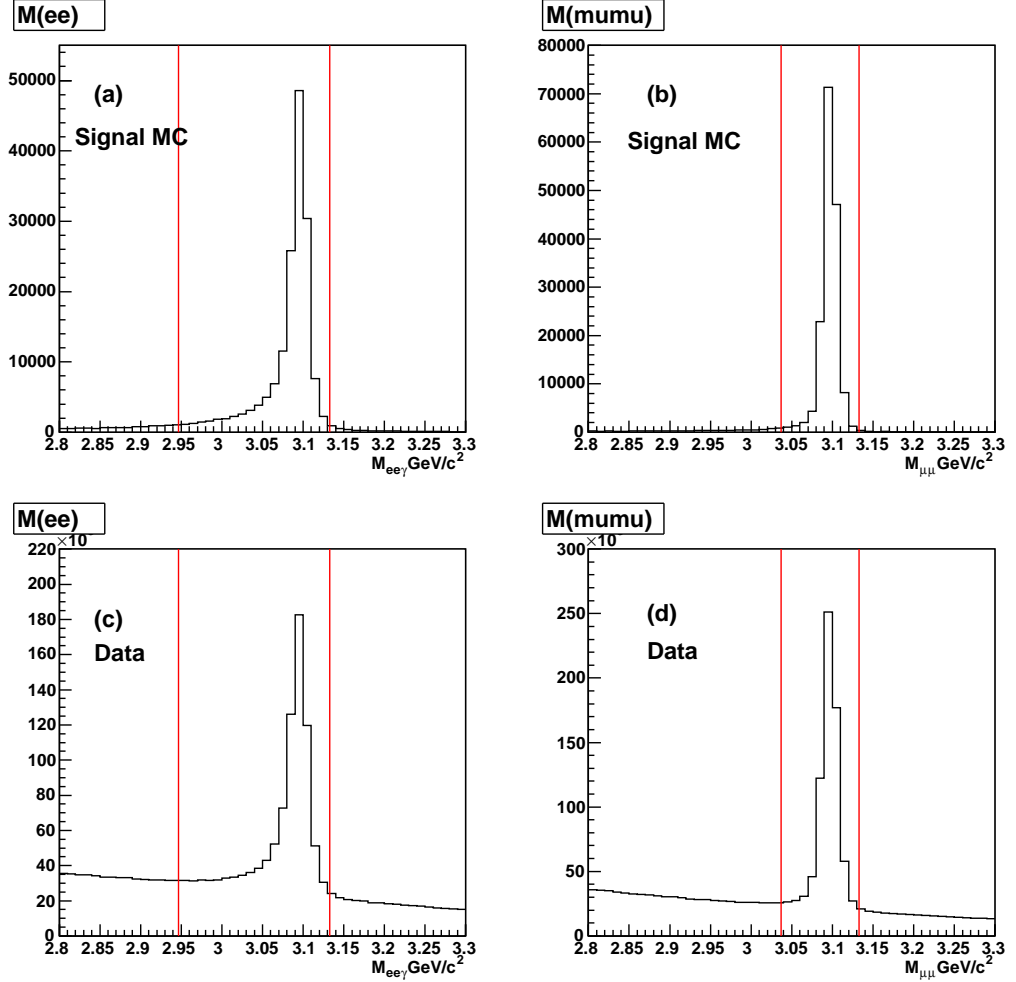


Figure 3.1: These are  $M_{J/\psi}$  distribution of signal MC and data. (a) is reconstructed from  $ee(\gamma)$  of signal MC. (b) is reconstructed from  $\mu\mu$  of signal MC. (c) is reconstructed from  $ee(\gamma)$  of data. (d) is reconstructed from  $\mu\mu$  of data. Red lines show invariant mass window boundaries to accept  $J/\psi$  candidates.

reconstructed  $\gamma$  is found to form the  $\pi^0$  candidate that is defined as  $0.117 \text{ GeV}/c^2 < M_{\gamma\gamma} < 0.153 \text{ GeV}/c^2$  by combining with any other photon, then this photon is rejected to from  $\eta$  candidates. And we determine  $\eta$  mass window as  $0.510 \text{ GeV}/c^2 < M_{\gamma\gamma} < 0.575 \text{ GeV}/c^2$  as indicated by vertical red

lines in Figure 3.2. Finally, in order to improve the momentum resolution of the  $\eta$ , mass constraint fit is applied.

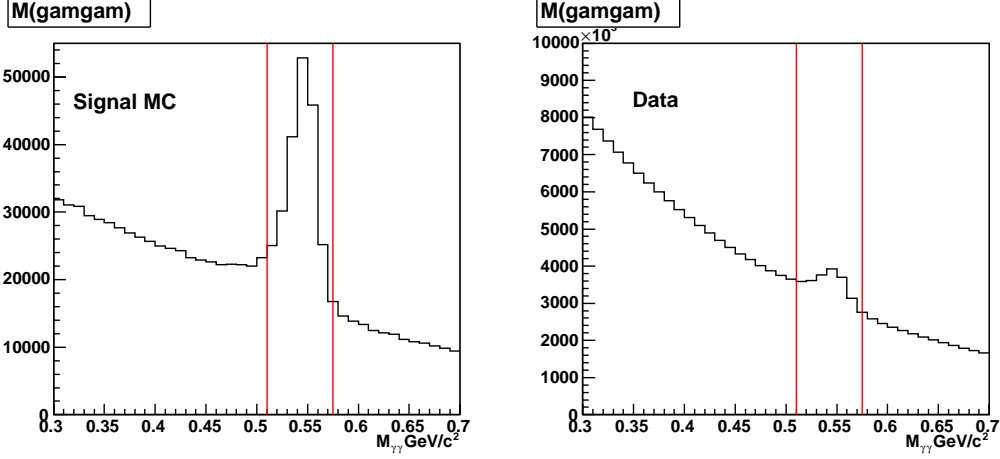


Figure 3.2: Mass distribution of  $\eta$  reconstructed from  $\gamma\gamma$ . Red lines show invariant mass window boundaries to accept  $\eta$  candidates.

### 3.2.8 $K/\pi$ identification

In order to distinguish charged kaons from pions, the sub-detectors of the Belle are able to provide information to compose a likelihood that a charged track is a kaon hypothesised or to be a pion. Then we can get the likelihood ratio as

$$P(K : \pi) = \frac{L_K}{L_K + L_\pi} \quad (3.2)$$

where  $L_i (i = K, \pi)$  is the product of the likelihoods that the particle is of type  $i$  and is calculated as,

$$L_i = L_i^{\text{CDC}} \times L_i^{\text{TOF}} \times L_i^{\text{ACC}} \quad (3.3)$$

For the reconstruction of  $B^\pm \rightarrow J/\psi\eta K^\pm$ ,  $K$  likelihood ratio is required to be larger than 0.4. And for the reconstruction of  $\psi' \rightarrow J/\psi\pi^+\pi^-$ , we required  $\pi$  likelihood ratio to be larger than 0.4, which is used for  $\psi'$  veto, it is explained in Section §4.2.1

### 3.2.9 $K_S^0$ reconstruction

For  $B^0 \rightarrow J/\psi\eta K_S^0$  candidate reconstruction,  $K_S^0$  is reconstructed by combining two oppositely charged pions. The two charged pion tracks are fitted with constraint to come from common vertex, and the pion pair invariant mass,  $M_{\pi^+\pi^-}$ , calculated at the obtained vertex is required to satisfy  $482 \text{ MeV}/c^2 < M_{\pi^+\pi^-} < 514 \text{ MeV}/c^2$ . The resultant momentum gotten by a mass- and vertex- fit is assigned to be the one for the reconstructed  $K_S^0$ .

## 3.3 Reconstruction of $B \rightarrow J/\psi\eta K$

To reconstruct  $B$  meson, the 2-body kinematics in the  $\Upsilon(4S) \rightarrow B\bar{B}$  is fully utilized. For the signal, the energy of reconstructed  $B$  in the centre-of-mass system (CMS),  $E_B^{\text{CMS}}$ , must be half the total energy of the  $e^+e^-$  system in the same frame,  $E_{\text{beam}}^{\text{CMS}}$ . With this constraint, the  $B$  meson candidate is identified by two kinematic variables defined as,

$$M_{\text{bc}} = \sqrt{(E_{\text{beam}}^{\text{CMS}})^2 - (p_B^{\text{CMS}})^2} \quad (3.4)$$

$$\Delta E = E_B^{\text{CMS}} - E_{\text{beam}}^{\text{CMS}} \quad (3.5)$$

The variable,  $M_{\text{bc}}$ , is known as the beam-constrained mass and peaks at the nominal  $B$  mass for correctly reconstructed case. The  $M_{\text{bc}}$  has much better resolution than the reconstructed  $B$  mass, thus providing better separation of signal and background. The energy difference,  $\Delta E$ , should peak around zero for correctly reconstructed  $B$  mesons. The  $B$  candidates satisfying  $M_{\text{bc}} > 5.2 \text{ GeV}/c^2$  and  $-0.2 \text{ GeV} < \Delta E < 0.2 \text{ GeV}$  are retained for further analysis. By the reconstruction procedure described so far, we find that 29% of the reconstructed events found in the region of  $M_{\text{bc}} > 5.2 \text{ GeV}/c^2$  and  $-0.2 \text{ GeV} < \Delta E < 0.2 \text{ GeV}$  have multiple  $B$  candidates. Most of the multiple candidates come from the different combination of  $\gamma\gamma$  when we reconstruct  $\eta$ . Smaller portion of multiple candidates come from lepton pair's combination at  $J/\psi$  reconstruction. Mistake of  $K^\pm$  or  $K_S^0$  selection would be more rare. The best candidate is selected when  $J/\psi$  and  $\eta$  are closest to the known candidate having least  $\chi^2$  is selected as best  $B$ , where  $\chi^2$  is defined as

$$\chi^2 = \left(\frac{M_{\ell\ell} - M_{J/\psi}}{\sigma_{J/\psi}}\right)^2 + \left(\frac{M_{\gamma\gamma} - M_\eta}{\sigma_\eta}\right)^2 \quad (3.6)$$

where,  $M_{\ell\ell}$  ( $M_{\gamma\gamma}$ ) is invariant mass which before the mass constraint is applied.  $M_{J/\psi}$  ( $M_\eta$ ) is the mass of  $J/\psi$  ( $\eta$ ) and  $\sigma_{J/\psi}$  ( $\sigma_\eta$ ) is mass resolution of  $J/\psi$  ( $\eta$ ). Where, each value is summarized as follows.

- $M_{J/\psi} = 3096.916 \text{ MeV}/c^2$
- $M_\eta = 547.853 \text{ MeV}/c^2$
- $\sigma_{J/\psi} (J/\psi \rightarrow e^+e^-) = 11.09 \text{ MeV}$
- $\sigma_{J/\psi} (J/\psi \rightarrow \mu^+\mu^-) = 8.9 \text{ MeV}$
- $\sigma_\eta (\eta \rightarrow \gamma\gamma) = 13.8 \text{ MeV}$

In very rare case, different  $K^\pm$  tracks can result in multiple candidates even though the  $J/\psi$  and the  $\eta$  candidates are identical. When it happens, we select the charged kaon having higher  $K$  likelihood ratio. In the same case for  $K_S^0$ , the one having the closest  $M_{\pi^+\pi^-}$  to the nominal  $K_S^0$  mass is chosen.

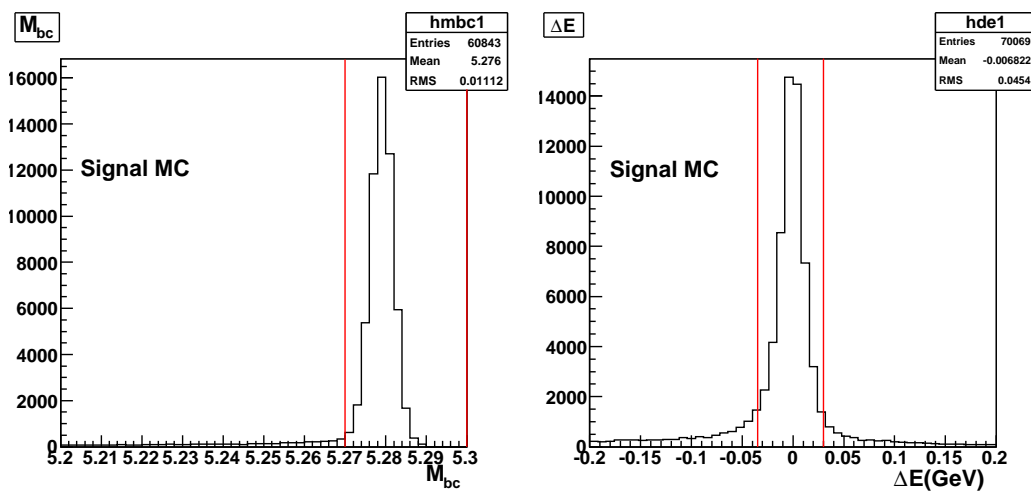


Figure 3.3:  $M_{bc}$  distribution in  $\Delta E$  signal region ( $-0.035 \text{ GeV} < \Delta E < 0.03 \text{ GeV}$ ) and  $\Delta E$  distribution in  $M_{bc}$  signal region ( $M_{bc} > 5.27 \text{ GeV}/c^2$ ) for  $B^\pm \rightarrow J/\psi\eta K^\pm$  PHSP MC sample.

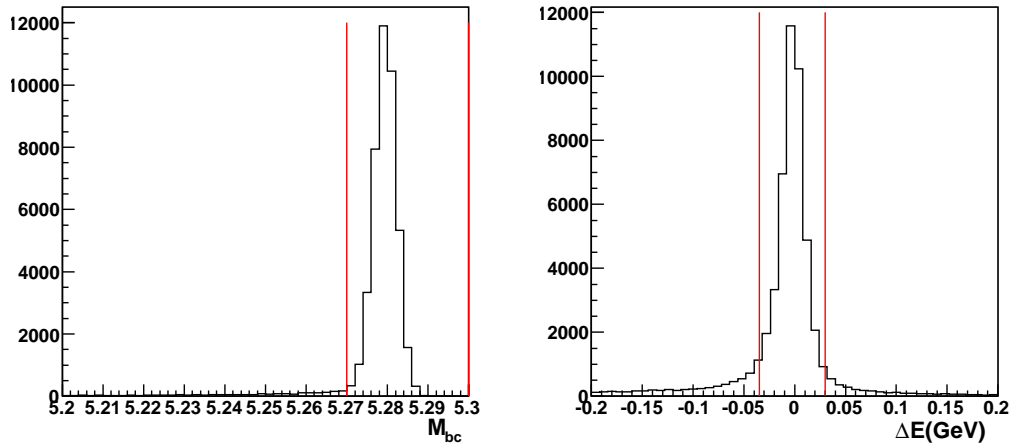


Figure 3.4:  $M_{bc}$  distribution in  $\Delta E$  signal region ( $-0.035 \text{ GeV} < \Delta E < 0.03 \text{ GeV}$ ) and  $\Delta E$  distribution in  $M_{bc}$  signal region ( $M_{bc} > 5.27 \text{ GeV}/c^2$ ) for  $B^0 \rightarrow J/\psi\eta K_S^0$  PHSP MC sample.

### 3.4 Detection efficiency of $B \rightarrow J/\psi\eta K$ decays

Based on the obtained  $M_{bc}$  and  $\Delta E$  distributions for the signal MC sample, we can estimate the detection efficiency by applying the same procedure to extract signal. We use unbinned maximum likelihood fit to  $\Delta E$  distribution, In order to perform it, an appropriate formula of the Probability Density Function (PDF) has to be found. Here, the  $\psi'$  veto, that is discussed in the next chapter for background reduction, is introduced.

#### 3.4.1 $B^\pm \rightarrow J/\psi\eta K^\pm$ mode

Since  $B^\pm \rightarrow J/\psi\eta K^\pm$  mode is expected to have enough statistics to attempt to resolve intermediate states, two MC samples are used to compose proper PDF for each,  $B^\pm \rightarrow J/\psi\eta K^\pm$  PHSP and  $B^\pm \rightarrow \psi'(\rightarrow J/\psi\eta)K^\pm$  processes. In both cases,  $\Delta E$  distribution is found to be well described by the double Gaussian which is sum of two Gaussians. In the PHSP case, the signal yield is found to be  $49593 \pm 239$  events in  $-0.2 \text{ GeV} < \Delta E < 0.2 \text{ GeV}$  out of 0.5 Million generated events. Integration of the obtained PDF in the range of  $-0.035 \text{ GeV} < \Delta E < 0.030 \text{ GeV}$  result in  $45624 \pm 220$  events to discuss about

the yield in  $B$  signal enhanced region to resolve intermediate states. Thus MC determined detection efficiency is 9.9% for  $-0.2 \text{ GeV} < \Delta E < 0.2 \text{ GeV}$  and 9.1% for  $-0.035 \text{ GeV} < \Delta E < 0.03 \text{ GeV}$ . Figure 3.5 shows fit to  $\Delta E$  distribution for signal PHSP MC. Here, small outlier component (green line in Figure 3.5) is introduced to fit large statistics signal MC sample. We omit this contribution from detection efficiency, because it is absorbed in background fluctuation.

Same procedure is repeated for  $B^\pm \rightarrow \psi'(\rightarrow J/\psi\eta)K^\pm$ .  $\Delta E$  distribution is obtained as shown in Figure 3.6. The MC determined detection efficiency of  $B^\pm \rightarrow \psi'K^\pm$  is estimated to be 9.4% at  $-0.2 \text{ GeV} < \Delta E < 0.2 \text{ GeV}$  and 8.5% at  $-0.035 \text{ GeV} < \Delta E < 0.030 \text{ GeV}$ . Note that in order to get the branching fraction from experimental data, the particle identification related correction factors must be multiplied to the MC determined efficiency to be discussed in Chapter 5.

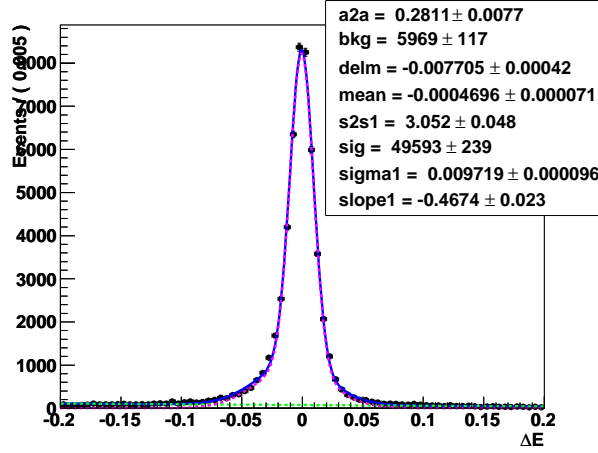


Figure 3.5: Fit to  $\Delta E$  (GeV) distribution for signal PHSP MC sample. The signal described by sum of two Gaussian and small outlier component (green dash line) are superimposed.

### 3.4.2 $B^0 \rightarrow J/\psi\eta K_S^0$ mode

Because of smaller expected statistics in  $B^0 \rightarrow J/\psi\eta K_S^0$  case, the study is performed only for the PHSP sample. We estimate the MC determined

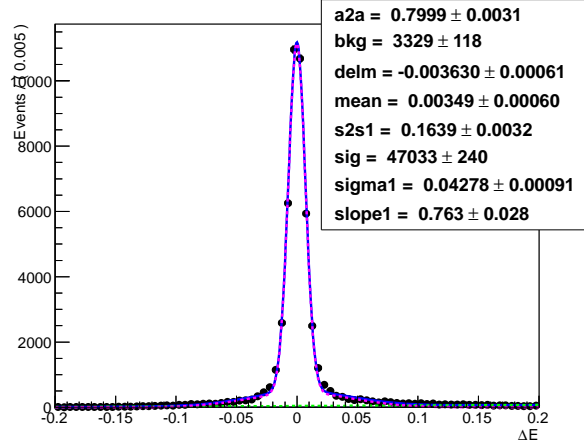


Figure 3.6: Fit to  $\Delta E$  (GeV) distribution of  $B^\pm \rightarrow \psi'(\rightarrow J/\psi\eta)K^\pm$  MC sample. Notation of the superimposed lines is same as Figure 3.5.

detection efficiency likewise charged mode. Figure 3.7 shows fit to  $\Delta E$  distribution for signal MC. The obtained MC determined efficiency is 8.1% for the  $B^0 \rightarrow J/\psi\eta K_S^0$  PHSP sample.

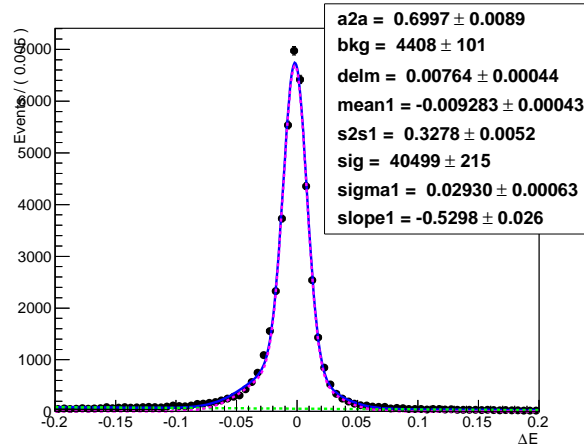


Figure 3.7: Fit to  $\Delta E$  (GeV) distribution of  $B^0 \rightarrow J/\psi\eta K_S^0$  PHSP MC sample. Notation of the superimposed lines is same as Figure 3.5.

# Chapter 4

## Background study

### 4.1 Continuum background reduction

To suppress the background coming from the continuum relative to  $B\bar{B}$  events, we use ratio of second to the zeroth Fox-Wolfram moments ( $R_2$ ).  $R_2$  is 0 for perfect spherical event.

$$R_2 = \frac{H_2}{H_0}, \quad H_t = \frac{\sum_{ij} |\vec{p}_i| |\vec{p}_j| P_t(\cos\theta_{ij})}{(\sum_i E_i)^2} \quad (4.1)$$

Here,  $P_t$  is the Legendre Polynomial and  $\vec{p}_i, \vec{p}_j$  represent the four momentum of the particles while  $\sum_i E_i$  represents the visible energy of the particles in the event. The  $B\bar{B}$  mesons are produced almost at rest and their decay axis are uncorrelated. So,  $B\bar{B}$  events are almost spherical in shape and can be distinguished from the jet like continuum events of  $u, d, s$  or  $c$ . To reduce the continuum background  $R_2$  is chosen to be less than 0.5.

### 4.2 Main backgrounds

For background study, we use the inclusive  $J/\psi$  MC sample corresponding to 100 times data larger statistics with respect to the used experiment data. Figure 4.1 (4.2) shows  $\Delta E$  distribution of the expected background along with the probable signal for  $B^\pm \rightarrow J/\psi\eta K^\pm$  ( $B^0 \rightarrow J/\psi\eta K_S^0$ ).

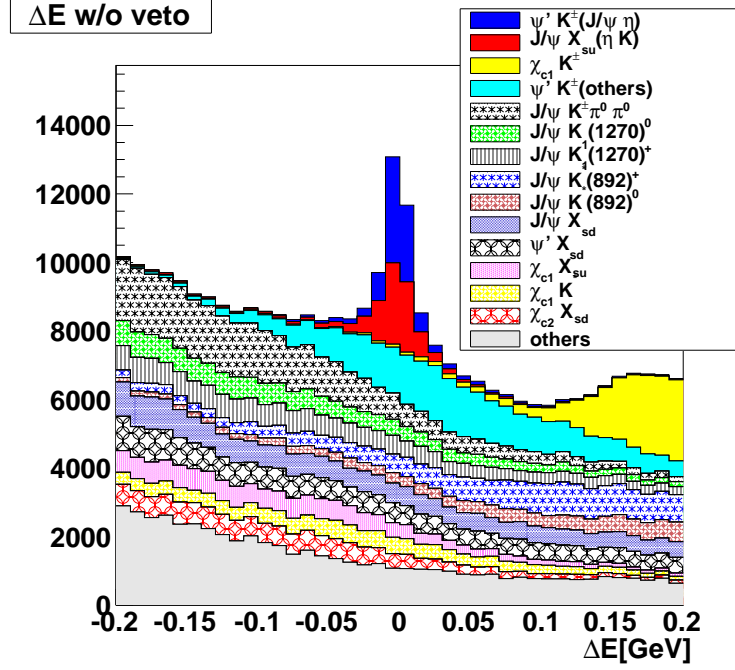


Figure 4.1: Expected  $\Delta E$  distribution of  $B^\pm \rightarrow J/\psi\eta K^\pm$  candidates for the inclusive  $J/\psi$  MC sample.

#### 4.2.1 $\psi' \rightarrow J/\psi\pi^+\pi^-$ and $\chi_{c1}(\chi_{c2}) \rightarrow \gamma J/\psi$ veto

We find  $B^\pm \rightarrow J/\psi\eta K^\pm$  ( $\psi' \not\rightarrow J/\psi\eta$ ) (light blue region in Figure 4.1) can be one of the backgrounds. Among  $\psi'$  decay modes into a  $J/\psi$ ,  $\psi' \rightarrow J/\psi\pi^+\pi^-$  has relatively large branching fraction, 33.6% and it is clearly identified. Therefore, we reject the  $J/\psi$  which come from  $\psi' \rightarrow J/\psi\pi^+\pi^-$  using mass difference cut  $0.58 \text{ GeV}/c^2 < M_{J/\psi\pi^+\pi^-} - M_{J/\psi} < 0.60 \text{ GeV}/c^2$ . Also, we found  $B^\pm \rightarrow \chi_{c1}K^\pm$  results in background above +0.1 GeV in  $\Delta E$  (yellow region in Figure 4.1), as this decay include  $\chi_{c1} \rightarrow J/\psi\gamma$ . So, we try to reject the  $J/\psi$  which coming from  $\chi_{c1} \rightarrow J/\psi\gamma$  using mass different cut  $0.39 \text{ GeV}/c^2 < M_{J/\psi\gamma} - M_{J/\psi} < 0.43 \text{ GeV}/c^2$ . Figure 4.3 shows mass difference of  $M_{J/\psi\pi^+\pi^-} - M_{J/\psi}$  and  $M_{J/\psi\gamma} - M_{J/\psi}$ . We can see one more peak in  $M_{J/\psi\gamma} - M_{J/\psi}$  distribution next to  $\chi_{c1} \rightarrow J/\psi\gamma$ . It is  $\chi_{c2} \rightarrow J/\psi\gamma$  and, we try to reject it also using mass difference cut  $0.45 \text{ GeV}/c^2 < M_{J/\psi\gamma} - M_{J/\psi}$

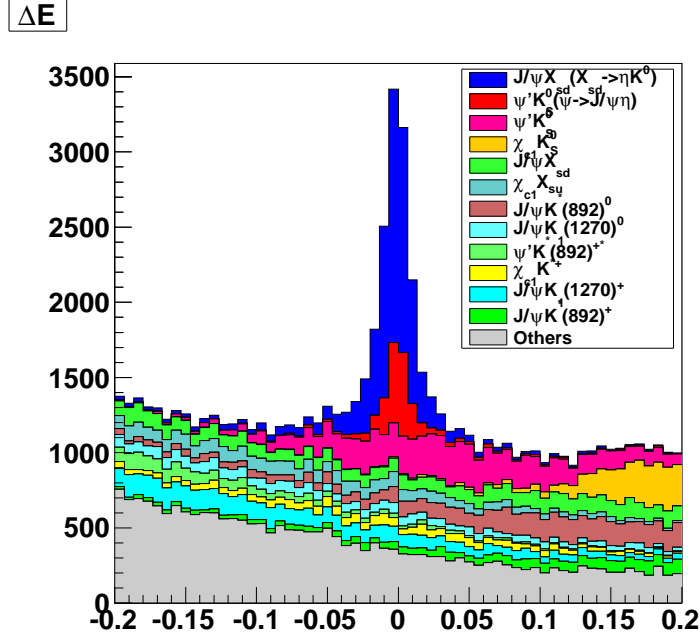


Figure 4.2: Expected  $\Delta E$  distribution of  $B^0 \rightarrow J/\psi\eta K_S^0$  candidates for the inclusive  $J/\psi$  MC sample. (After applying the  $\psi' \rightarrow J/\psi\pi^+\pi^-$  veto, that is to be mentioned in the text.)

$< 0.48 \text{ GeV}/c^2$ . Whether these vetos are effective is judged by the figure of merit (F.O.M.) defined as

$$\text{F.O.M.} = \frac{N_S}{\sqrt{N_S + N_B}} \quad (4.2)$$

$$N_S = \epsilon \times \mathcal{B} \times N_{B\bar{B}} \quad (4.3)$$

where,  $N_S$  is the number of expected signal events and,  $N_B$  is the number of expected background.  $\mathcal{B}$  is the product of the branching fractions of  $B^\pm \rightarrow J/\psi\eta K^\pm$ ,  $J/\psi \rightarrow \ell^+\ell^-$  and  $\eta \rightarrow \gamma\gamma$  decay chain.  $\epsilon$  is the detection efficiency of  $B^\pm \rightarrow J/\psi\eta K^\pm$ . Table 4.1 summarizes the F.O.M. study based on the mentioned vetos. Signal loss is found to be unacceptably large in  $\chi_{c1,c2}$  veto, and result in deterioration of the F.O.M. On the other hand,  $\psi'$  veto gives

almost some F.O.M. as the case without any veto and it will make the  $\psi'$  background related uncertainty small. Thus, only  $\psi'$  veto is to be applied.

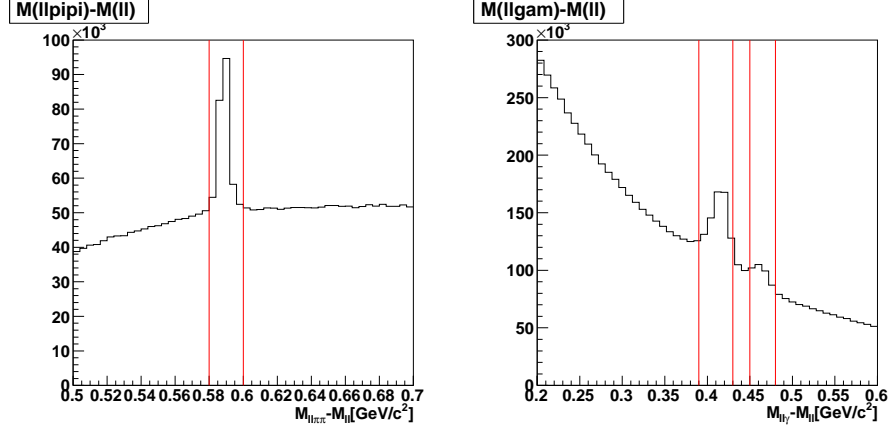


Figure 4.3: Mass difference of  $M_{J/\psi\pi\pi} - M_{J/\psi}$  for  $\psi' \rightarrow J/\psi\pi^+\pi^-$  veto (left).  $M_{\gamma J/\psi} - M_{J/\psi}$  for  $\chi_{c1}(\chi_{c2}) \rightarrow J/\psi\gamma$  vetos (right). The vertical lines show the window to apply vetos.

Mode	$N_S$	$N_B$	$N_S/N_B$	F.O.M.
Without veto	448.79	759.25	0.59	12.91
All veto	288.31	345.38	0.83	11.45
$\psi'$ veto	422.01	649.07	0.65	12.89
$\chi_{c1}$ veto	356.38	649.07	0.71	12.16
$\chi_{c2}$ veto	386.68	632.3	0.61	12.11
$\chi_{c1}$ and $\chi_{c2}$ veto	304.11	411.43	0.74	11.37
$\chi_{c1}$ and $\psi'$ veto	335.87	425.79	0.79	12.16

Table 4.1: F.O.M. study for each veto.

## 4.2.2 Non $J/\psi$ background

We checked non- $J/\psi$  background, i.e. due to fake  $J/\psi$ , using  $e^+e^-(\gamma)$  or  $\mu^+\mu^-$  mass sideband of the  $J/\psi$  signal region (Figure 3.1) in the experimental data.

- $M_{ee(\gamma)}$  :  $2.80 \text{ GeV}/c^2 < M_{ee(\gamma)} < 2.95 \text{ GeV}/c^2$  and  $3.13 \text{ GeV}/c^2 < M_{ee(\gamma)} < 3.30 \text{ GeV}/c^2$  .
- $M_{\mu\mu}$  :  $2.80 \text{ GeV}/c^2 < M_{\mu\mu} < 3.03 \text{ GeV}/c^2$  and  $3.13 \text{ GeV}/c^2 < M_{ee(\gamma)} < 3.30 \text{ GeV}/c^2$  .

As shown in Figure 4.4, non- $J/\psi$  background is small and has flat distribution in  $\Delta E$  projection. Here, the inclusive  $J/\psi$  MC is normalized to data, and sideband data is normalized to the signal region. Non- $J/\psi$  background is found to be enough small and to be treated as apart of combinatrial background.

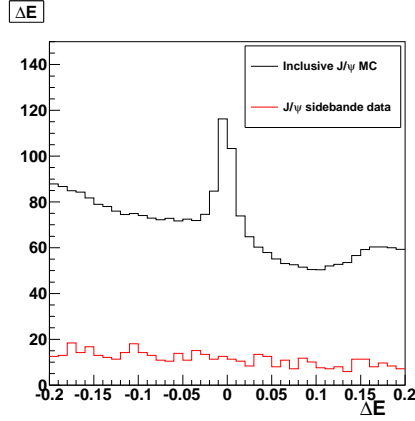


Figure 4.4: Comparing between inclusive  $J/\psi$  MC (black) and non- $J/\psi$  background (red).

### 4.3 Optimization of $\Delta E$ window

After extracting the  $B$  decay signal, the  $J/\psi\eta$  invariant mass distribution is to be visited. In order to have the proper  $B$  candidate sample for this purpose, the  $\Delta E$  window should be optimized. The optimum window is judged by the F.O.M. using the signal PHSP MC and the inclusive  $J/\psi$  MC sample. It shows optimum for  $\Delta E$  lower and upper bounds at  $-0.025 \text{ GeV}$  and  $+0.020 \text{ GeV}$  respectively. F.O.M. plots are shown in Figure 4.5. However, concerning the possible  $\Delta E$  resolution difference between data and MC,  $-0.035 \text{ GeV} < \Delta E < +0.030 \text{ GeV}$  is to be used.

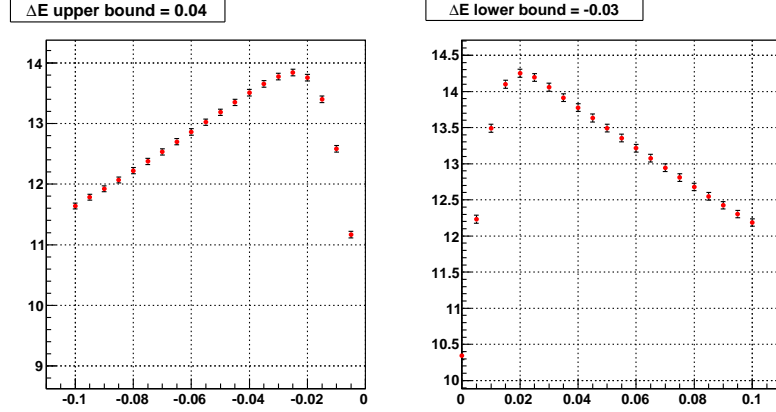


Figure 4.5: F.O.M. is shown as a function of  $\Delta E$  lower bound with fixing  $\Delta E$  upper bound = 0.04 GeV (left) and  $\Delta E$  upper bound with  $\Delta E$  lower bound = -0.03 GeV (right).

## 4.4 Background probability density functions

As seen in Figure 4.1,  $B^\pm \rightarrow \chi_{c1} K^\pm$  and  $B^\pm \rightarrow \psi' K^\pm$  have nontrivial structure in  $\Delta E$  distribution in  $B^\pm \rightarrow J/\psi \eta K^\pm$  case. Same things happen also in the case of  $B^0 \rightarrow J/\psi \eta K_S^0$  as shown in Figure 4.2. In order to parameterize them, we used bifurcated Gaussian as shown in Figure 4.6. Since rest of backgrounds are featureless, we used 2nd order polynomial for  $B^\pm \rightarrow J/\psi \eta K^\pm$  candidates and 1st order polynomial for  $B^0 \rightarrow J/\psi \eta K_S^0$ . The treatment of the latter case is to have stable fit even in the limited statistics.

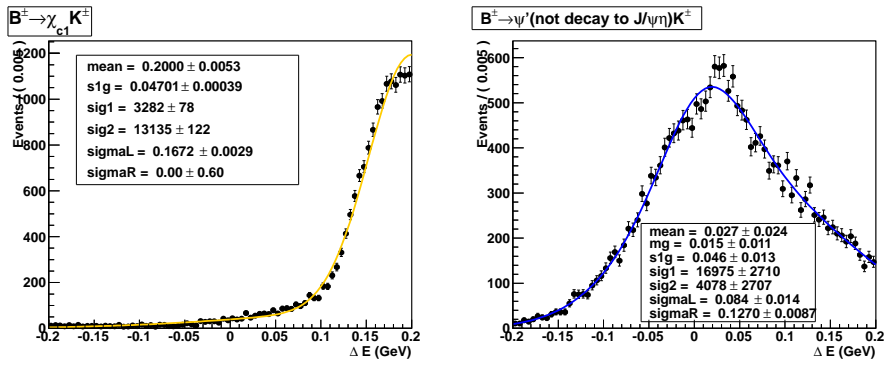


Figure 4.6:  $\Delta E$  distributions for  $B^\pm \rightarrow \chi_{c1} K^\pm$  and  $B^\pm \rightarrow \psi' (\not\rightarrow J/\psi\eta) K^\pm$  background with fitted by Bifurcated Gaussian. For  $B^0 \rightarrow \chi_{c1} K_S^0$  and  $B^0 \rightarrow \psi' (\not\rightarrow J/\psi\eta) K_S^0$  backgrounds, same procedure is applied.



# Chapter 5

## Results and discussions

### 5.1 $B$ decay signal extraction

Using the signal and backgrounds probability density functions (PDFs) described in the previous chapters, the  $B$  decay signal is extracted by an unbinned maximum likelihood fit to  $\Delta E$  distribution. The fit program was tested by the pseudo-experiments using either GEANT based simulation sample or a parameterized MC (called Toy MC) sample and no significant bias was found. Figure 5.1 the fit to the  $\Delta E$  distribution for  $B^\pm \rightarrow J/\psi\eta K^\pm$  and  $B^0 \rightarrow J/\psi\eta K_S^0$  decay modes in the range of  $[-0.2, 0.2]$  GeV. We observe  $428 \pm 37$  events for  $B^\pm \rightarrow J/\psi\eta K^\pm$  decay and  $80 \pm 14$  for  $B^0 \rightarrow J/\psi\eta K_S^0$  decay. The statistical significance is defined as  $\sqrt{-2\ln L_o/L_{\max}}$ , where  $L_{\max}$  and  $L_o$  are the likelihood values when maximized by allowing the signal yield vary and in the case to set to zero, respectively. We find  $B^\pm \rightarrow J/\psi\eta K^\pm$  shows  $17.9\sigma$  and  $B^0 \rightarrow J/\psi\eta K_S^0$  exhibits  $7.1\sigma$  statistical significance.

### 5.2 Resolving intermediate states by $M_{J/\psi\eta}$ distribution

Since we find the  $B^\pm \rightarrow J/\psi\eta K$  signal yield has enough statistics, the invariant mass of  $J/\psi\eta$  system,  $M_{J/\psi\eta}$ , is used to resolve the intermediate states in this three-body decay. As discussed in Chapter 4, the  $\Delta E$  window,  $-0.035$  GeV  $< \Delta E < +0.030$  GeV is chosen as the optimum. Inside this  $\Delta E$  window,  $403 \pm 35$  events of  $B^\pm \rightarrow J/\psi\eta K^\pm$  signal is contained. The  $M_{J/\psi\eta}$

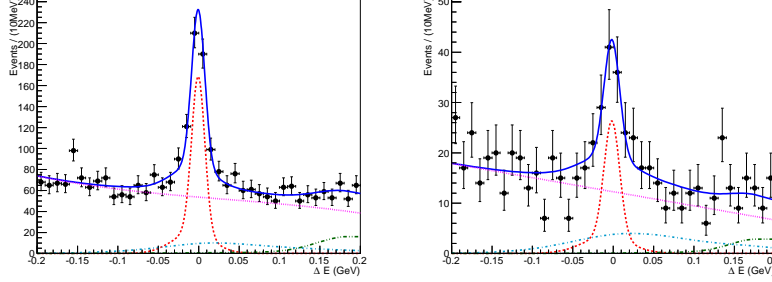


Figure 5.1:  $\Delta E$  distribution of  $B^\pm \rightarrow J/\psi\eta K^\pm$  and  $B^0 \rightarrow J/\psi\eta K_S^0$  candidate in  $5.27 \text{ GeV}/c^2 < M_{bc} < 5.29 \text{ GeV}/c^2$ . Left is charged mode, and right is neutral mode. Dash line with red is signal's PDF, dot-dash line with cyan is  $B \rightarrow \psi'(\rightarrow J/\psi\eta)K$ 's PDF, dot-dot-dash line with green is  $B \rightarrow \chi_{c1}K$ 's PDF and dot line with pink is other backgrounds.

distribution for the candidates selected by applying the  $\Delta E$  window requirement is shown in Figure 5.2. At  $3686 \text{ MeV}/c^2$ , the  $\psi' \rightarrow J/\psi\eta$  contribution is clearly seen. However, there is no other significant peak. The signal yield of  $B^\pm \rightarrow \psi'K^\pm$  and  $\psi' \rightarrow J/\psi\eta$  decay chain process is found to be  $46 \pm 8$  events and this process is denoted as  $B^\pm \rightarrow (\psi' \rightarrow J/\psi\eta)K^\pm$  hereafter. The  $M_{J/\psi\eta}$  distribution for  $\psi' \rightarrow J/\psi\eta$  signal is expressed by a double Gaussian and other contribution is described by a threshold function. By subtracting this contribution from the total  $B^\pm \rightarrow J/\psi\eta K^\pm$  signal, the signal yield excluding  $B^\pm \rightarrow (\psi' \rightarrow J/\psi\eta)K^\pm$  is found to be  $357 \pm 38$  events. Since this contribution shows a phase space like distribution, we use  $B^\pm \rightarrow J/\psi\eta K^\pm(\text{PHSP})$  to denote it. Based on the MC determined efficiencies described in chapter 3, taking the correction factors of charged particle identification, the detection efficiency,  $\epsilon$ , is estimated to be 8.7%, 8.0% and 7.5% for  $B^\pm \rightarrow J/\psi\eta K^\pm$  PHSP,  $B^\pm \rightarrow \psi'(\rightarrow J/\psi\eta)K^\pm$  and  $B^0 \rightarrow J/\psi\eta K_S^0$ , respectively. Table 5.1 summarizes these results and we get total three-body branching fractions for charged and neutral  $B$  mesons;

$$\mathcal{B}(B^\pm \rightarrow J/\psi\eta K^\pm) = (1.3 \pm 0.1(\text{stat.}) \pm 0.1(\text{syst.})) \times 10^{-4} \quad (5.1)$$

$$\mathcal{B}(B^0 \rightarrow J/\psi\eta K_S^0) = (4.3 \pm 0.7(\text{stat.}) \pm 0.4(\text{syst.})) \times 10^{-5} \quad (5.2)$$

where, systematic error estimation is described in the following subsection.

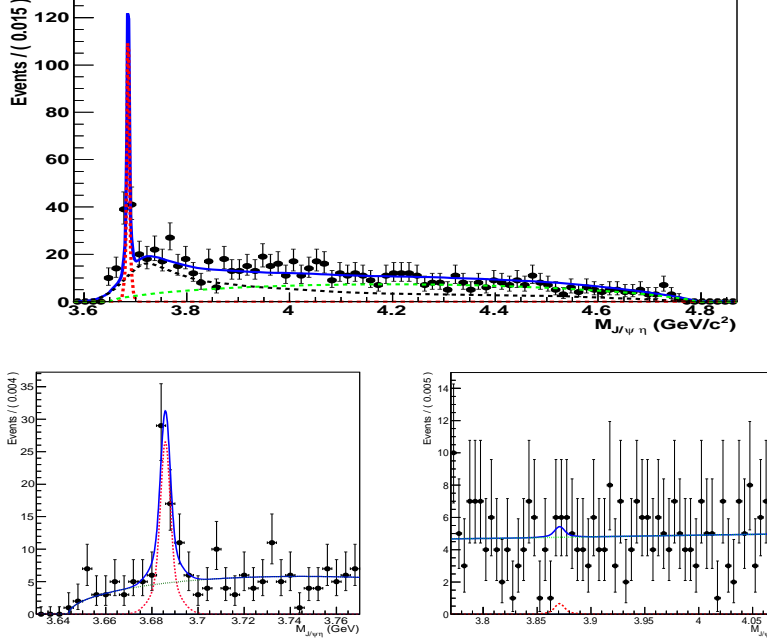


Figure 5.2: The  $J/\psi\eta$  mass ( $M_{J/\psi\eta}$ ) distribution for  $B^\pm \rightarrow J/\psi\eta K^\pm$  candidates. All kinematically allowed region (upper), and  $\psi'$  (lower, left) and  $X(3872)$  (lower, right) regions are shown.

## 5.3 Correction and systematic uncertainties

This section explains the estimation of the correction for possible difference between data and MC and systematic uncertainties.

### 5.3.1 Tracking efficiency systematic

To estimate tracking efficiency systematic the decay chain of  $D^{*+} \rightarrow \pi^+ D^0$ ,  $D^0 \rightarrow \pi^+ \pi^- K_S^0$  and  $K_S^0 \rightarrow \pi^+ \pi^-$  is reconstructed. The  $K_S^0$  is required to decay inside the first SVD layer and one pion from  $K_S^0$  is allowed not to be explicitly detected. We call it the partially reconstructed sample. The  $D^{*+}$  signal yield in the case of both  $K_S^0$  daughter pions are detected is compared to the partially reconstructed sample and the difference between data and MC gives the correction and systematic uncertainty. This correction is  $(-0.13 \pm$

Table 5.1: Summary of branching fractions. Only statistical error is quoted.

Decay	$\epsilon(\%)$	Yield	Branching fraction
$B^\pm \rightarrow J/\psi\eta K^\pm$ (Total)	8.7	$403 \pm 35$	$(1.3 \pm 0.1) \times 10^{-4}$
$B^\pm \rightarrow \psi'(\rightarrow J/\psi\eta) K^\pm$	8.0	$46 \pm 8$	$(0.2 \pm 0.03) \times 10^{-4}$
$B^\pm \rightarrow J/\psi\eta K^\pm$ (PHSP)	8.7	$357 \pm 38$	$(1.1 \pm 0.1) \times 10^{-4}$
$B^0 \rightarrow J/\psi\eta K_S^0$	7.5	$80 \pm 14$	$(4.3 \pm 0.7) \times 10^{-5}$

$0.30 \pm 0.10$ )% per track.

### 5.3.2 Correction and systematic uncertainty of $K$ ID

The decay chain of  $D^{*+} \rightarrow \pi^+ D^0$ ,  $D^0 \rightarrow K^- \pi^+$  and its charge conjugate reaction are used to calibrate charged identification efficiency. In this decay chain,  $D$  meson daughter  $K$  and  $\pi$  always have opposite and same charge sign with respect to the slow  $\pi$  from  $D^*$ . The number of kaon tracks satisfying the identification requirement are compared between data and MC.  $K$  ID correction and uncertainty are found to be  $1.0064 \pm 0.0138$ /track.

### 5.3.3 Correction and systematic uncertainty of $\mu$ ID

The lepton pair production in two photon collisions,  $e^+e^- \rightarrow e^+e^-\mu^+\mu^-$  is useful to calibrate  $\mu$ -on identification efficiency. Because of the singularity in the QED, either  $e^+$  or  $e^-$  is likely to escape from detection by going along with beampipe, while  $\mu$ -ons can have enough transverse momentum to be detected. The events in the case where only one  $\mu$ -on track is explicitly identified is called "Single tag", on the other hand "Double tag" denotes the events where both  $\mu$ -ons are positively identified. The ratio between "Single tag" and "Double tag" events are compared between data and MC. Same procedure is repeated to an inclusive  $J/\psi \rightarrow \mu\mu$  sample for validation. As a result,  $\mu$  ID efficiency correction and uncertainty are found to be  $0.937 \pm 0.037$  for the case both  $J/\psi$  daughters are required to be identified.

### 5.3.4 Electron ID correction and systematic uncertainty

In order to check electron ID systematic, we use an inclusive  $J/\psi \rightarrow e^+e^-(\gamma)$  sample. We define two cases for  $J/\psi$  reconstruction :

1. Single tag : when one electron has  $L_e > 0.9$  while other has no condition applied for the identification.
2. Double tag : when one electron has  $L_e > 0.9$  and other has  $L_e > 0.01$ .

Similarly to  $\mu$ ID case, the ratio between single-tag yield and double tag yield is compared between data and MC. As a result, we estimate electron ID correction and uncertainty as  $0.9516 \pm 0.0082$  for the case both  $J/\psi$  daughters are required to be identified.

### 5.3.5 $\eta$ detection systematic uncertainty

For  $\eta \rightarrow \gamma\gamma$  decay's systematic, the ratio of the signal yields for  $\eta \rightarrow \gamma\gamma$  and  $\eta \rightarrow \pi^0\pi^0\pi^0$  are compared between data and MC. As a result, we assign 4.0% as the uncertainty.

### 5.3.6 Correction and systematic uncertainty of $K_S^0 \pi^+ \pi^-$ detection

In order to estimate  $K_S^0 \rightarrow \pi^+ \pi^-$  samples. One is selected by "loose" and the other is "tight". The "loose" sample is collection of the oppositely charged pion pairs without any special requirement on each track with very wide invariant mass window from  $350 \text{ MeV}/c^2$  up to  $650 \text{ MeV}/c^2$ . Among these pion pairs, the proper  $K_S^0 \rightarrow \pi^+ \pi^-$  selection criteria are applied to have the "tight" sample.

The ratio between the signal yield in "tight" sample and "loose" sample's number of events is compared between data and MC. As a result, the correction factor for efficiency of  $K_S^0 \rightarrow \pi^+ \pi^-$  detection as well as its uncertainty are obtained to be  $0.9879 \pm 0.0073$ .

### 5.3.7 Signal MC statistics

Our detection efficiency estimation is based on the signal MC samples with 0.5 Million events. Statistical error of these samples result in 0.5% for  $B$  decay branching fractions.

### 5.3.8 Number of $B$ meson pairs

This systematic is due to the uncertainty on the number of  $B$  meson pairs,  $N_{B\bar{B}}$ , for experimented data. It is obtained to be  $(771.58 \pm 10.6) \times 10^6$  which gives a systematic uncertainty of 1.4%.

### 5.3.9 Branching fraction uncertainties

We are using secondary branching fractions such as  $J/\psi \rightarrow e^+e^-$  or  $\mu\mu$ ,  $\eta \rightarrow \gamma\gamma$  and  $K_S^0 \rightarrow \pi^+\pi^-$ . Uncertainty of these secondary branching fractions are taken into account as summarized in Table 5.2.

Decay mode	Branting ratio	Uncertainty (%)
$J/\psi \rightarrow e^+e^-$	$0.0594 \pm 0.0006$	1.01
$J/\psi \rightarrow \mu^+\mu^-$	$0.0593 \pm 0.0006$	1.01
$J/\psi \rightarrow \ell^+\ell^-$ (Combining above two)	$0.1187 \pm 0.0008$	0.7
$\eta \rightarrow \gamma\gamma$	$0.39 \pm 0.0020$	0.51

Table 5.2: Summary of secondary branching fractions and uncertainties.

### 5.3.10 PDF systematic uncertainties

We extract signal yield by performing a fit to data. Our signal yield depends upon the parameter fixed in the fit. We may have uncertainty from the modeling of the different components for the distribution (PDF). For this purpose we repeat fits by varying the fixed parameters of the PDF by  $\pm 1\sigma$  to see the variation of results. From this procedure, we estimate the PDF uncertainty for  $B^\pm \rightarrow J/\psi\eta K^\pm$ ,  $B^\pm \rightarrow \psi'(\rightarrow J/\psi\eta)K^\pm$  and  $B^0 \rightarrow J/\psi\eta K_S^0$  as 7.3%, 3.9% and 8.4%, respectively.

### 5.3.11 Summary of systematic uncertainties

The systematic uncertainty estimated by the procedures described above is summarized in the Table 5.3.

	$B^\pm \rightarrow J/\psi\eta K^\pm$	$B^\pm \rightarrow \psi'(\rightarrow J/\psi\eta)K^\pm$	$B^0 \rightarrow J/\psi\eta K_S^0$
Tracking	0.9	0.9	1.3
$K$ ID	1.4	1.4	N/A
Lepton ID	2.4	2.4	2.4
$\eta \rightarrow \gamma\gamma$ detection	4.0	4.0	4.0
$K_S^0 \rightarrow \pi^+\pi^-$	N/A	N/A	0.7
Signal MC state	0.5	0.5	0.5
Secondary Br.	0.7	0.7	0.7
PDF uncertainty	7.3	3.9	8.4
	8.9%	6.4%	9.8%

Table 5.3: Summary of systematic uncertainty of branching fraction. Here, lepton ID is 3.9% for  $\mu$ , 0.4% for  $e$  and averaged effect is quoted in the Table.

## 5.4 Upper limit for resonance in $J/\psi\eta$ final state

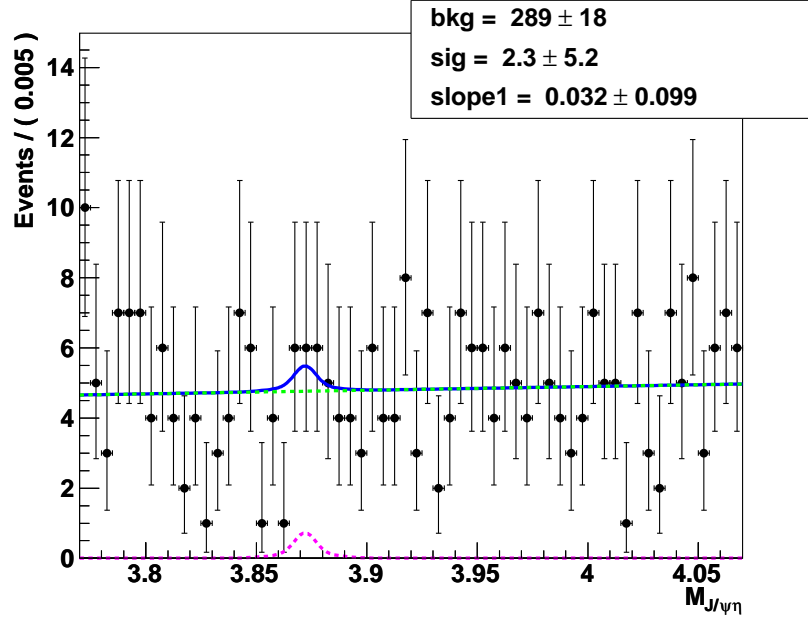
Based on the fact that we found no significant peak in  $M_{J/\psi\eta}$  distribution except for the well known state  $\psi'$ , we calculate the upper limit on the product of branching fraction at 90% confidence level using a frequentist approach. We provide upper limits for  $X(3872)$ ,  $\psi(3770)$  and narrow resonance (hypothesis at 4020 MeV/ $c^2$ , 4220 MeV/ $c^2$ , 4420 MeV/ $c^2$  and 4620 MeV/ $c^2$ ).

### 5.4.1 $X(3872)$

We fit data at  $X(3872)$  as shown in Fig 5.3. The signal PDF is determined by the signal MC with setting width to be zero. We get signal yeild to be  $2.3 \pm 5.2$  events. Therefore we get  $\mathcal{Br}(B^\pm \rightarrow X(3872)K^\pm)\mathcal{Br}(X(3872) \rightarrow J/\psi\eta) < 3.8 \times 10^{-6}$ .

### 5.4.2 Narrow resonances at other mass points

We repeat same procedure for narrow resonance at other mass points. The narrow resonances visited mass points are 4020 MeV/ $c^2$ , 4020 MeV/ $c^2$ , 4220 MeV/ $c^2$ , 4420 MeV/ $c^2$  and 4620 MeV/ $c^2$ . The upper limit at 90% C.L. is estimated same approach as  $X(3872)$  case. Table 5.4 and Figure 5.4 show

Figure 5.3: Fit result of  $M_{J/\psi\eta}$  distribution at  $X(3872)$  region.

summary of upper limit.

Resonance	Efficiency(%)	Yield(90% C.L.)	$Br(\times 10^{-6})$
$X(3872)$	8.12	10.6	3.8
$X(4070)$	9.75	10.5	3.1
$X(4270)$	9.79	9.2	2.7
$X(4470)$	9.43	17.25	5.3
$X(4670)$	8.4	7.0	2.4

Table 5.4: Summary of the obtained upper limits for the product of branching fractions.

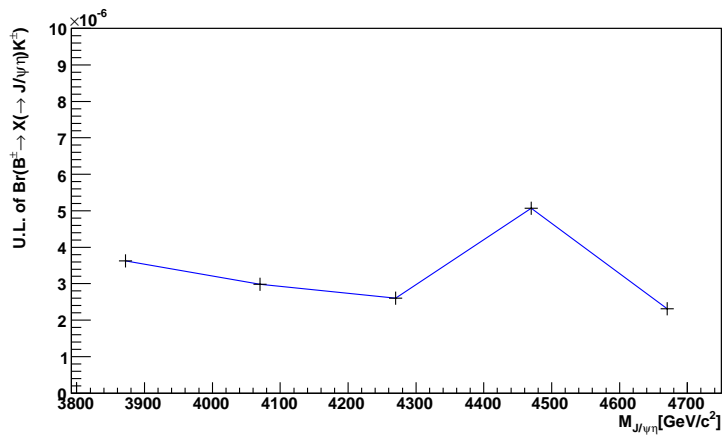


Figure 5.4: U.L. (@ 90% C.L.) on the  $\mathcal{B}(B^\pm \rightarrow XK^\pm) \cdot \mathcal{B}(X \rightarrow J/\psi\eta)$  estimated at different masses using narrow width hypothesis.



# Chapter 6

## Summary

We observed  $B^\pm \rightarrow J/\psi\eta K^\pm$  signal yield as  $428 \pm 37$  events from Belle data corresponding to 772  $B\bar{B}$  pair. In this  $B$  decay sample, the fit to  $M_{J/\psi\eta}$  distribution tells that  $\psi' \rightarrow J/\psi\eta$  signal yield is  $44.3 \pm 8.1$  events. Otherwise, the  $B$  decay signal event show phase space like distribution thus we do not have any signiture of a narrow resonance in  $J/\psi\eta$  final state. As a consequence, we get  $\mathcal{B}(B^\pm \rightarrow X(3872)K^\pm) \cdot \mathcal{B}(X(3872) \rightarrow J/\psi\eta) < 3.8 \times 10^{-6}$ .

We reconstructed  $B^0 \rightarrow J/\psi\eta K_S^0$  and its signal yield is obtained to be  $80 \pm 14$  events. As a result, we present

$$\begin{aligned}\mathcal{B}(B^\pm \rightarrow J/\psi\eta K^\pm) &= (1.3 \pm 0.1(\text{stat}) \pm 0.1(\text{syst})) \times 10^{-4} \\ \mathcal{B}(B^0 \rightarrow J/\psi\eta K_S^0) &= (4.3 \pm 0.7(\text{stat}) \pm 0.4(\text{syst})) \times 10^{-5}.\end{aligned}$$



# Bibliography

- [1] M. Kobayashi, and T. Masukawa, Prog. Theor. Phys. **49**, 652 (1973).
- [2] D. Gross, and F. Wilczek, Phys. Rev. Lett. **30**, 1343 (1973). H. politzer, Phys. Rev. Lett. **30**, 1346 (1973).
- [3] L. Wolfenstein, Phys. Rev. Lett. **51**, 1945 (1983)
- [4] S.-K. Choi, S. L. Olsen *et al.* (Belle Collaboration), Phys. Rev. Lett. **91**, 262001 (2003).
- [5] T. Nakano *et al.* (LEPS Collaboration), Phys. Rev. Lett. **91**, 012002 (2003).
- [6] S. K. Choi, S. L. Olsen *et al.* (Belle Collaboration), Phys. Rev. Lett. **91**, 261801 (2003).
- [7] B. Aubert *et al.* (BaBar Collaboration), Phys. Rev. Lett. **93**, 041801 (2004).
- [8] V. Bhardwaj *et al.* (Belle Collaboration), Phys. Rev. Lett. **107**, 091803 (2011).
- [9] B. Aubert *et al.* (BaBar Collaboration), Phys. Rev. Lett. **102**, 132001 (2009).
- [10] R. L. Jaffe, Phys. Rev. D. **15**, 267 (1977).
- [11] L. Maiani *et al.*, Phys. Rev. Lett. **93**, 212002 (2004).
- [12] K. Terasaki, Prog. Theor. Phys. **127**, 577-582 (2012).
- [13] S. Godfrey and S. L. Olsen, Annu., Rev. Nucl. Part. Sci. **58**, 51-73 (2008).

- [14] G. V. Pakhlova, P. N. Pakhlov, Eidel'sman, *Physics Uspekhi* **53** (3) 249-241
- [15] N. Isgur, J. E. Paton, *Phys. Rev. D.* **31**, 2910 (1985).
- [16] T. Branes, F. E. Close, E.S. Swanson, *Phys. Rev. D.* **52**, 5242 (1995).  
P. Lacock, C. Michael, P. Boyle, P. Rowland (UKQCD Collaboration), *Phys. Rev. B.* **401**, 308 (1997).  
X. Liao and T. manke, arXiv:021003v2 [hep-lat]
- [17] F. Close, Three flavours of hybrid or pi exchange: Which is more attractive? In Proc. Int. Conf. Hadron Spectrosc., 12th , Frascati, Italy, Oct. 8-13, 2007. hep-ph:0801.2646 (2008)
- [18] M. B. Voloshin, arXiv:0602233 [hep-ph] (2006)
- [19] D. Acosta *et al.* (CDF Collaboration), *Phys. Rev. Lett.* **93**, 072001 (2004).
- [20] V.M. Abazov *et al.*, (D0 Collaboration), *Phys. Rev. Lett.* **93**, 162002 (2004).
- [21] R.Aaij *et al* (LHCb Collaboration), *Eur Phys. J. C.* **72**, 1972 (2012).
- [22] B. Aubert *et al.* (BaBar Collaboration), *Phys. Rev. D.* **71**, 071103 (2005).
- [23] National Laboratory for High Energy Physics. "KEKB *B*-factory Design Report", *Phys. Rev. D* **43**, 2193 (1993).
- [24] A. Abashian *et al.* (The Belle Collaboration), *Nucl. Instr. and Meth. A* **479**, 117 (2002).
- [25] V. Chabaud *et al.* *Nucl. Instr. and Meth. A* **368**, 314 (1996).
- [26] Belle Collaboration, S. K. Choi, S. L. Olsen, K. Trabelsi *et al.*, *Phys. Rev. D* **84**, 052004 (2011).
- [27] A. Abulencia *et al.*, (CDF Collaboration), *Phys. Rev. Lett* **98**, 132002 (2007).
- [28] T. Aushev, N. Zwahlen *et al.*, (Belle Collaboration), *Phys. Rev. D* **81**, 031103 (2010).

- [29] E. Braaten and J. Stapleton, Phys. Rev. D **81**, 014019 (2010).
- [30] C. Bignamini, B. Grinstein, F. Piccinini, A. D. Polosa, C. Sabelli, Phys. Rev. Lett **103**, 162001 (2009).
- [31] B. Aubert *et al.* (BaBar Collaboration), Phys. Rev. D **71**, 031501 (2005).
- [32] K. Terasaki, Prog. Theor. Phys. **127** 577-582 (2012).
- [33] D. J. Lange, Nucl. Instr. and Meth. **A462**, 152 (2001).
- [34] R. Brune *et al.*, “GEANT 3.21”, CERN DD/EE/84-1 (1984).